




Review

Photo-Thermal Dry Reforming of Methane with PGM-Free and PGM-Based Catalysts: A Review

Alessio Varotto ^{1,2,*}, Umberto Pasqual Laverdura ¹ , Marta Feroci ²  and Maria Luisa Grilli ^{1,*} 

¹ Energy Technologies and Renewable Sources Department, Italian National Agency for New Technologies, Energy and Sustainable Economic Development (ENEA), Via Anguillarese 301, 00123 Rome, Italy; umberto.pasqual@enea.it

² Department of Fundamental and Applied Sciences for Engineering (SBAI), Sapienza University of Rome, Via Castro Laurenziano, 7, 00161 Rome, Italy; marta.feroci@uniroma1.it

* Correspondence: alessio.varotto@uniroma1.it (A.V.); marialuisa.grilli@enea.it (M.L.G.)

Abstract: Dry reforming of methane (DRM) is considered one of the most promising technologies for efficient greenhouse gas management thanks to the fact that through this reaction, it is possible to reduce CO₂ and CH₄ to obtain syngas, a mixture of H₂ and CO, with a suitable ratio for the Fischer-Tropsch production of long-chain hydrocarbons. Two other main processes can yield H₂ from CH₄, i.e., Steam Reforming of Methane (SRM) and Partial Oxidation of Methane (POM), even though, not having CO₂ as a reagent, they are considered less green. Recently, scientists' challenge is to overcome the many drawbacks of DRM reactions, i.e., the use of precious metal-based catalysts, the high temperatures of the process, metal particle sintering and carbon deposition on the catalysts' surfaces. To overcome these issues, one proposed solution is to implement photo-thermal dry reforming of methane in which irradiation with light is used in combination with heating to improve the efficiency of the process. In this paper, we review the work of several groups aiming to investigate the pivotal promoting role of light radiation in DRM. Focus is also placed on the catalysts' design and the progress needed for bringing DRM to an industrial scale.

Keywords: photo-thermal; dry reforming of methane; platinum group metals (PGMs); PGM-based catalysts; PGM-free catalysts; syngas



check for updates

Citation: Varotto, A.; Pasqual Laverdura, U.; Feroci, M.; Grilli, M.L. Photo-Thermal Dry Reforming of Methane with PGM-Free and PGM-Based Catalysts: A Review. *Materials* **2024**, *17*, 3809. <https://doi.org/10.3390/ma17153809>

Academic Editor: Aivaras Kareiva

Received: 17 June 2024

Revised: 18 July 2024

Accepted: 22 July 2024

Published: 1 August 2024



Copyright: © 2024 by the authors. Licensee MDPI, Basel, Switzerland. This article is an open access article distributed under the terms and conditions of the Creative Commons Attribution (CC BY) license (<https://creativecommons.org/licenses/by/4.0/>).

1. Introduction

Currently, there is an increasing concentration of greenhouse gases (GHGs) in the atmosphere caused by anthropogenic activities, leading to global warming [1], especially due to CO₂ and CH₄. Correlations between the annual increase in temperature and GHGs have been analyzed over the years by many research centers, including NASA [2–4]. Figure 1 shows the chart of global temperature anomalies, which are deviations from a reference value or long-term average, and the increasing CO₂ emissions in the period from 1959 to 2022. Despite the ten-year variation of some tenths of degrees, it must be considered that even 1 or 2 °C can have a huge impact on the global environment [5].

The escalating levels of CO₂ and CH₄ concentrations in the atmosphere have intensified concerns regarding climate change [6]. The Paris Agreement was signed by 196 parties who committed to reduce GHG emissions to limit global warming well below 2 °C above pre-industrial levels, increasing the ability to adapt to the adverse impacts of climate change and create forest climate resilience and low-GHG-emission development [7]. The target goals are to reduce CO₂ emissions by at least 30 gigatons (Gt_{CO₂})/yr [8] using alternative energy sources and, at the same time, employing carbon capture, utilization and storage (CCUS), reducing costs and increasing energy efficiency. Europe must achieve these goals by 2030 to reduce GHG emissions, and this is part of the “Fit for 55” legislation that is part of the European Green Deal to achieve climate neutrality by 2050. During the last COP28 (Conference of the Parties) in Dubai, more than 200 parties discussed the world’s

first “global stock-take” to ratchet up climate change action before the end of the decade, with the overarching aim to keep the global temperature increase below 1.5 °C. One of the most important points of this COP is that the agreement on mitigation measures now includes a fossil fuel phase-out instead of only a phase-down. This is the first COP in which fossil fuels were designated as the principal cause of climate change.

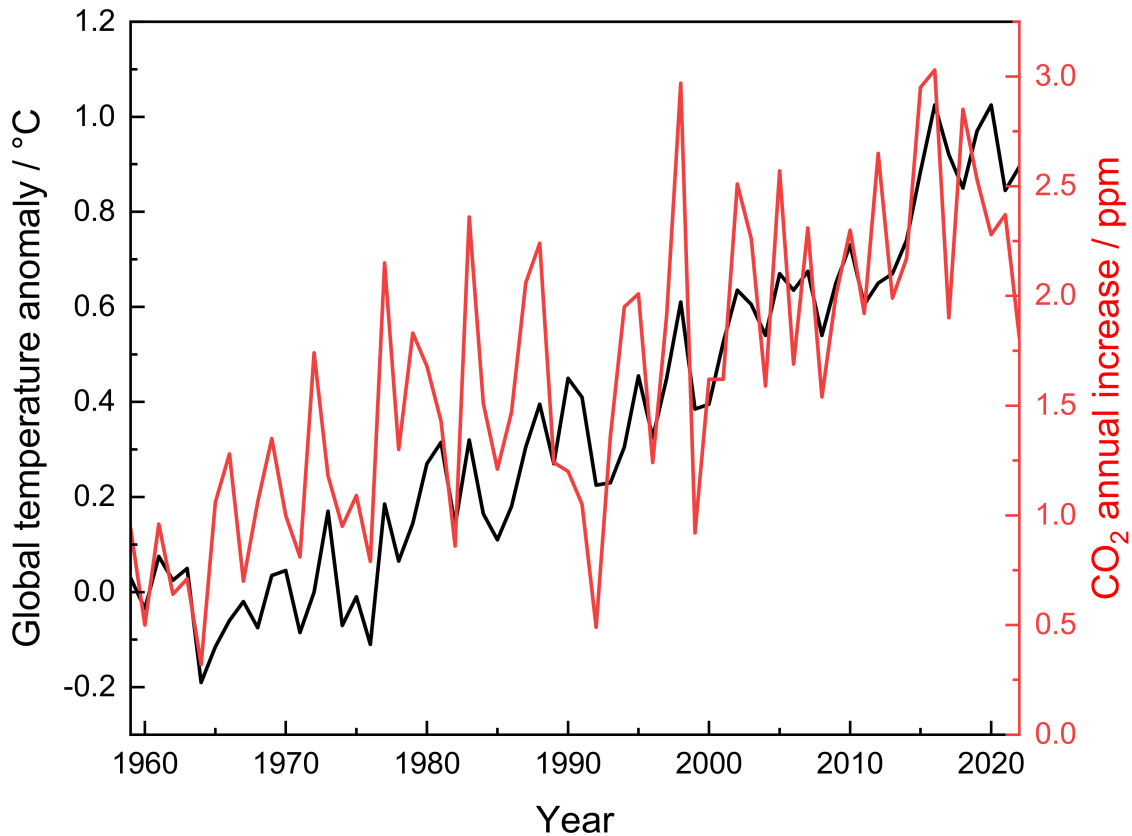


Figure 1. The link between increasing global temperature and increasing CO₂ emissions from 1859 to 2022. The data are taken from ref. [5].

Dry reforming of methane (DRM) constitutes a valuable approach for effective CO₂ and CH₄ conversion to added-value syngas (H₂ and CO), even though it is considered at present to be far from effectively mitigating the environmental issues related to GHG emissions because of the many challenges limiting its widespread application at the industrial scale.

Many review papers on dry reforming of methane reactions can be found in the literature and are focused on particular aspects, such as the catalysts’ active materials, the supports, the catalysts’ design, the catalysts’ deactivation by carbon deposition, etc. With this review paper on photo-thermal dry reforming of methane preceded by only a few previous ones [9–16], we aim to investigate the pivoting role of light irradiation focusing both on platinum group metal-free catalysts and catalysts containing platinum group metals as active elements.

This review will start with a description of the dry reforming of methane reaction, followed by a description of the other reactions forming syngas from methane (bi- and tri-reforming of methane). The principles of photo-thermal catalysis (PTC) will be introduced before the photo-thermal dry reforming of methane (PTC-DRM) description, with PTC-DRM being the focus of the present paper. Then, the catalysts for PTC-DRM, both containing platinum group metals (PGMs) and without PGMs, will be reviewed.

2. Dry Reforming of Methane (DRM) Reaction

In the dry reforming of methane, CO₂ and CH₄ react to obtain a syngas rich in CO and H₂ [17]. The DRM reaction was studied for the first time by Fischer and Tropsch in 1928 using nickel and cobalt catalysts, and nowadays, it is proposed as a potential solution to convert CO₂ on a large scale [8,18]. Equation (1) reports the DRM reaction and Figure 2 schematizes the DRM reaction promoted by a source of heat. The main characteristics of the DRM are that, according to the thermodynamics [19], it may yield a H₂/CO ratio close to unity and is highly endothermic, so high temperatures (>650 °C) must be used to promote the DRM reaction, even in the presence of a catalyst [18].

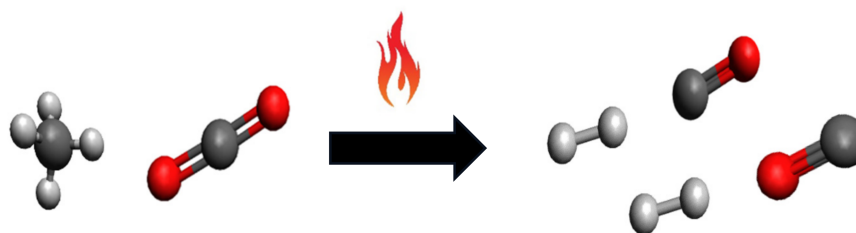
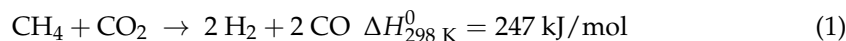


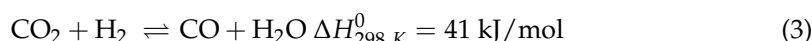
Figure 2. DRM reaction promoted by a source of heat.

As the variation in enthalpy is positive, for Le Chatelier's principle, high temperatures are needed to transform the reagents into syngas, as evident from the Gibbs Equation (2) [19–21]:

$$\Delta G_f^0 = \Delta H_f^0 - \Delta S_f^0 \times T \quad (2)$$

where ΔH_f^0 is the variation in enthalpy formation, equal to 247 kJ/mol, and ΔS_f^0 is the variation in entropy formation, equal to 0.26 kJ/(mol·K) [22]. ΔG_f^0 is negative when $T > 950 \text{ K}$ [23].

It is important to underline that the H₂/CO ratio in the DRM reaction is always lower than unity due to the reverse water gas shift (RWGS) equilibrium reaction (3):



where part of the hydrogen formed during the DRM reaction reacts with carbon dioxide to form carbon monoxide and water [24]. Equations (1) and (3) are spontaneous when the temperature is above 650 °C, and this means that the RWGS is inevitable [25].

High temperatures are needed because of the high energies required to break the first C-H bond in methane (750 kJ/mol), which is the rate-determining step of the entire reaction, and the first C=O bond in carbon dioxide (476 kJ/mol).

To decrease the activation energies and thus the temperature needed to promote the DRM reaction, catalysts are generally used. The reaction can also be promoted by using external sources of light. Thus, as schematized in Figure 3, the DRM reaction can occur thermocatalytically (TC), photocatalytically (PC) and photothermocatalytically (PTC).

The first classical method employs heat to promote the DRM reaction, the second one uses a light source, typically a Xe or a Hg lamp or a concentrated sunlight, and in the third one, both heat and light are combined to increase the efficiency of the reaction. The last approach, i.e., the synergistic effect of light and heat, seems to be more powerful than the sum of its parts [26–29].

In the following sections, the fundamentals of photo-thermal (applying the principles of PC and TC) dry reforming of methane will be discussed [24,30–33]. Photo-thermal dry reforming of methane is superior compared to the other two pathways proposed; for thermocatalysis occurring at high temperatures (the reaction is endothermic), byproducts such as coke may be generated, and only an opportune catalyst design can mitigate the

effect of catalyst deactivation by carbon deposition. At low temperatures, even if carbon deposition is reduced, to achieve high catalytic efficiencies, the assistance of a light source is necessary. On the other hand, a light source without heat assistance does not lead to high catalytic efficiency. Therefore, temperature plays a significant role in the DRM reaction, as reported by many authors. As an example, Sokefun et al. [33] have investigated the effect of Ru loading and reduction temperature of Ru-Ni-Mg/Ceria-Zirconia catalysts, achieving dry reforming activity between 450 and 510 °C, even though conversion efficiencies were lower in comparison to the values generally obtained at higher temperatures.

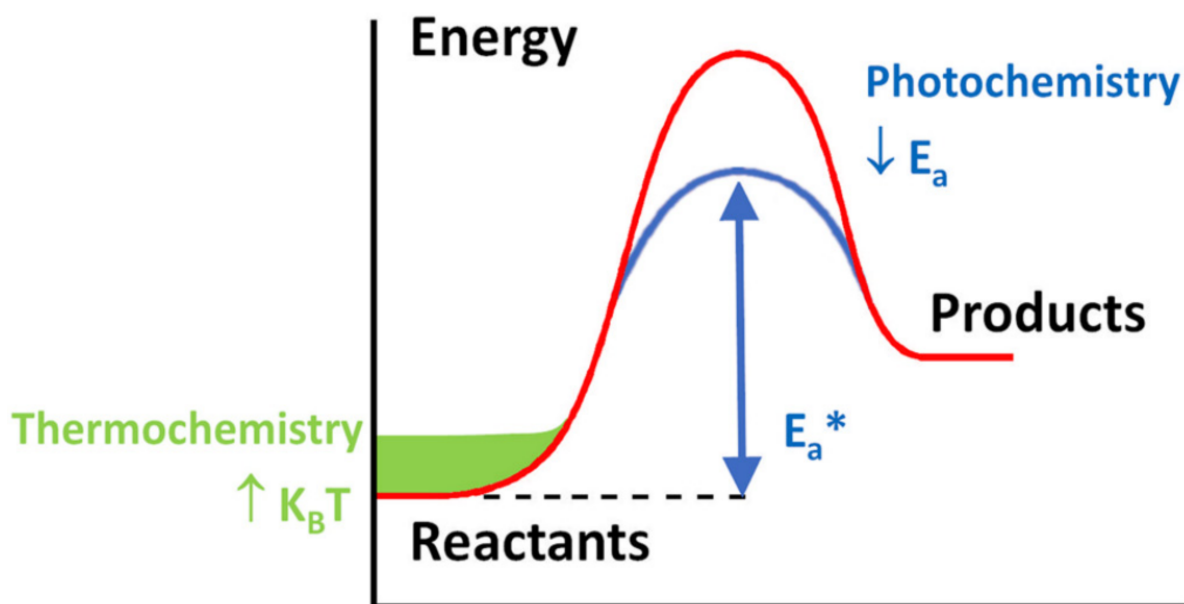
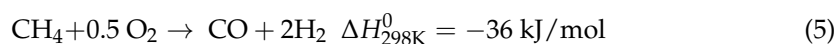
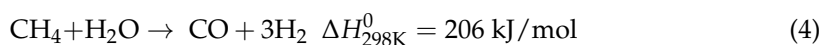


Figure 3. Photo-catalysis and thermo-catalysis contributions to PTC. During photo-catalysis, the activation energy barrier (E_a , red line) is reduced by the effect of light (E_a^* , blue line), while the temperature effect is to provide additional thermal energy ($k_B T$, green zone) to the energy path of an endothermic reaction. Figure reprinted with permission from [34]. Adapted from [35]. Copyright 2008 Royal Society of Chemistry.

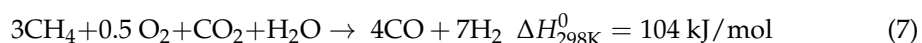
3. Bi- and Tri-Reforming of Methane

The DRM reaction converts the two GHGs CH_4 and CO_2 into syngas; however, two other main reactions can be used to convert methane into syngas: Steam Reforming of Methane (SRM) and Partial Oxidation of Methane (POM), which are reported in Equations (4) and (5):



The SRM reaction provides syngas from methane and water, while the POM reaction uses oxygen in place of H_2O [36].

When Equations (1) and (4) are combined together, in one step (6), the process is called bi-reforming of methane (BRM) or CS DRM (i.e., combined SRM and DRM). When Equations (1), (4) and (5) are combined together, in one step, the process is called tri-reforming of methane (TRM) (7).



BRM enhances the H₂ production using SRM, due to the equilibrium in the water gas shift reaction. The combination of dry reforming with steam reforming leads to a syngas with flexible H₂/CO ratios via easy adjustment of feed-stock composition and suitable for the Fisher–Tropsch production of methanol, oxo-alcohols and other chemicals. In addition, in BRM, carbon deposition on catalysts' surface [37] is reduced.

Tahir et al. [38] synthesized a Co/HC₃N₄ catalyst with different Co loading and performed a photo-activity test using a Hg lamp with light intensity of 100 mW/cm² at different feed mixtures of CH₄/CO₂. HC₃N₄ was used because of its ability to exploit solar energy, while cobalt was used to increase the active sites and capture the charge carriers. The highest production rates of H₂ and CO were obtained in the case when 2% wt. of Co was used, reaching 689 and 95.8 μmol/g, respectively, after 4 h of irradiation time. In both DRM and BRM reactions, production rate decreased in the presence of water.

As in a DRM reaction, in a TRM reaction, oxides such as CeO₂, ZrO₂ and MgO are also generally used [39]. Due to the presence of CO₂ as a reactant, support needs a high oxygen storage capacity, as it increases the conversion of carbon dioxide due to the basic character of these oxides [40]. Oxide supports are chosen due to their high thermal stability and their high oxygen storage capacity, and it is even possible to use them as photocatalysts for one of these reactions.

Despite BRM and TRM showing very promising potential because of their higher H₂/CO ratios and reduced carbon deposition on catalysts' surface, several challenges, as in DRM, exist for their scalability [37].

Figure 4 reports the trends of publications about DRM, PTC-DRM, BRM and TRM starting from 1994, and ref. [41] reports a bibliometric study on dry reforming of methane.

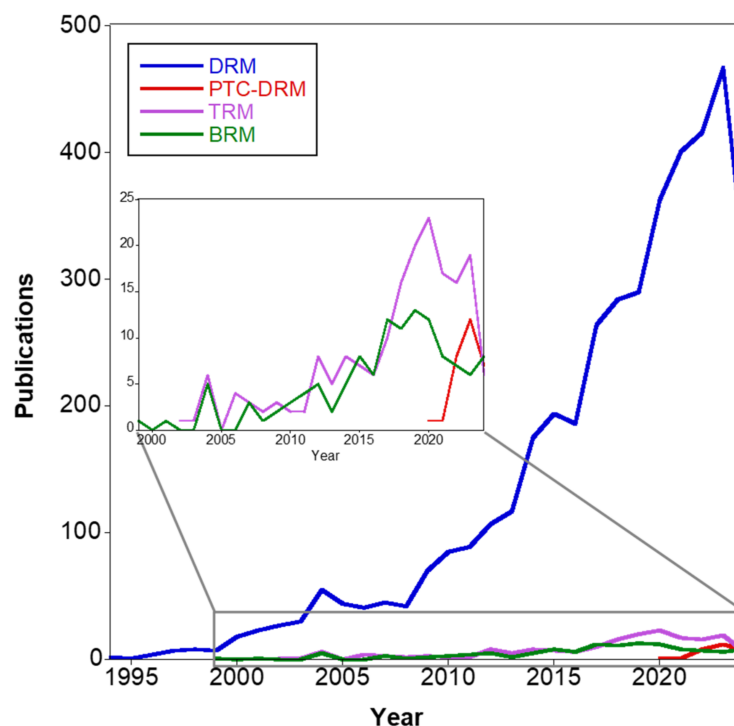


Figure 4. Publications trends over the years of “DRM”, “PTC-DRM”, “BRM” and “TDRM” (source: Scopus: 5 July 2024).

4. Fundamentals of Photo-Thermal Catalysis

In this section, the focus is on the fundamentals of Photo-Thermal Catalysis (PTC) to analyze how catalysts' performances are improved by light absorption. In PTC, absorption of photons by a material promotes electrons from the valence to the conduction band and generates electron–hole pairs, which will participate in the subsequent redox reactions.

PTC involves the interaction between photons, electrons and phonons, giving rise to photo-thermal and/or Localized Surface Plasmon Resonance (LSPR) effects [42,43].

While PTC utilizes lattice vibrations induced by light to achieve the photo-thermal conversion, the LSPR mechanism generates an electric field enhancement by plasmons and it utilizes electron dispersion to generate hot carriers, i.e., charge carriers (electrons) that dissipate energy in the form of heat. The LSPR mechanism occurs when resonant conditions are satisfied, i.e., when the energy of the external source of light matches the work function of the metal nanoparticles on the surface. In this way, resonant frequencies of conduction electrons and incident electromagnetic waves are enhanced on the surface of plasmonic nanoparticles, in so-called hot spots. The excess energy can decay through several pathways, radiative or non-radiative. In non-radiative decay, electrons will generate hot charge carriers in the plasmonic structure through intra- (s-to-s transitions) or interband (d-to-s transitions) mechanisms (this phenomenon is called “Landau damping”). In this case, electron–hole pair excitations and electron–electron collisions occur. To facilitate the promotion of electrons from the valence band to the conduction band, it is important to use materials with a narrow band gap. In fact, one of the main challenges in photo-catalysis is to avoid electron–hole recombination to facilitate the formation of products [44,45]. For plasmon-induced catalysis, several reaction mechanisms have been proposed on the basis of their time scale with or without an adsorbate or a semiconductor (Figure 5) [46].

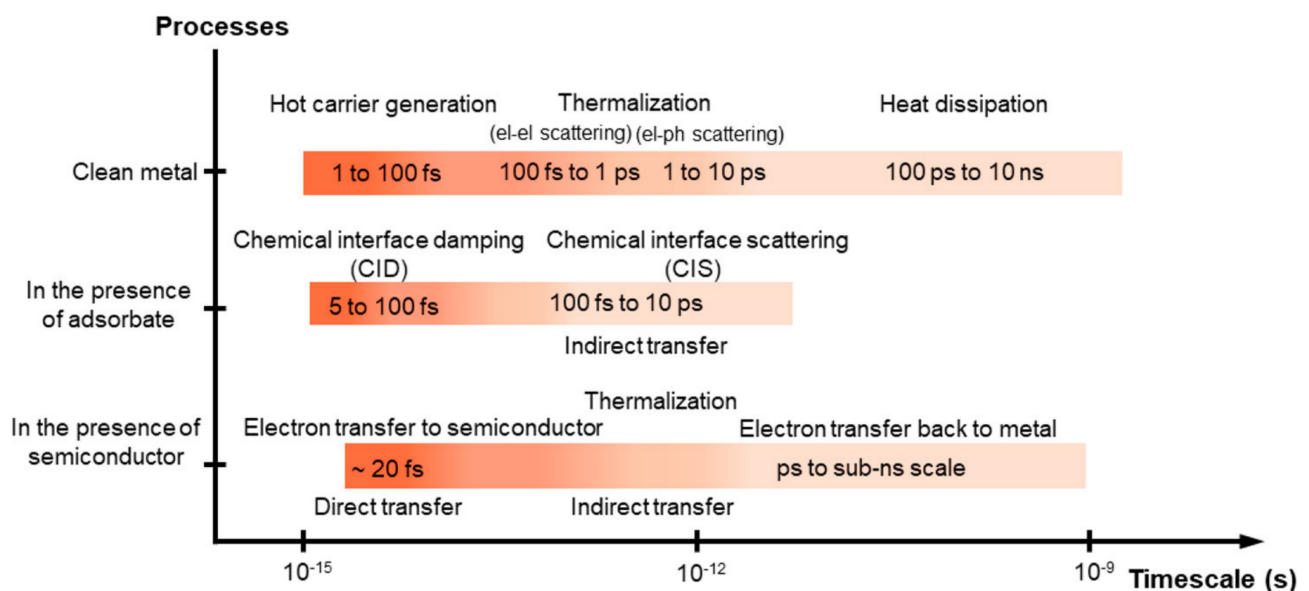


Figure 5. Time scales of plasmon-induced hot carrier generation, hot electron transfer, and thermalization processes. Figure reprinted with permission from [46].

Indirect and direct hot electron transfer (HET) into a semiconductor is the topic of a very recent review [45]. In Figure 6, the indirect and direct charge transfer (CT) mechanisms are represented in the case of a plasmon-induced catalysis. The indirect electron transfer is a two-step process. In the first step, hot carriers (electrons and holes) are generated, while in the second one, there is the transfer of electrons and, depending on the existence of a single-component or a hetero-structured plasmonic photocatalyst, this can happen through a metal/adsorbate system (Figure 6a) or a metal/semiconductor system (Figure 6b,c). In the latter case, the electron transfer occurs through a Schottky barrier and the trapping of the transferred hot electrons increases their lifetime, because they do not travel back to the metal nanostructure.

The disadvantage of indirect electron transfer is the necessity to have electrons near the Fermi level. On the contrary, direct electron transfer is a single-step process, and it is assumed that energy loss is lower. However, high electric fields are needed for the direct electron transfer process to occur.

More insights about PTC are available in the literature [28,44–50].

In a reaction process involving light excitation, the efficiency η defined in (8) and the quantum efficiency Q.E. defined in (9) must be considered:

$$\eta = \frac{(r_{CO} \times \Delta_c H_{CO}^0 + r_{H_2} \times \Delta_c H_{H_2}^0 - r_{CH_4} \times \Delta_c H_{CH_4}^0)}{P_{illumination}} \times 100\% \quad (8)$$

where $P_{illumination}$ is the light power used, r_i represents the reaction rate, $\Delta_c H_i^0$ is the standard combustion heat and i represents products and reagents, with $\Delta_c H_{CO_2}^0$ being equal to zero.

$$Q.E. = \frac{\text{the number of reacted electrons (n)}}{\text{the number of incident photons (N)}} \times 100\% \quad (9)$$

The quantum efficiency Q.E. is the ratio of the reacted electrons and the number of incident photons N, which can be calculated using (10):

$$N = \frac{I \times S \times t \times \lambda}{hc} \quad (10)$$

where I is the light power per area, S the surface area, t the time during which the catalyst is exposed to the light source, λ the wavelength, h the Planck's constant and c the velocity of light [51].

In the next paragraph, the synergistic effect of light and heat on the DRM reaction will be discussed.

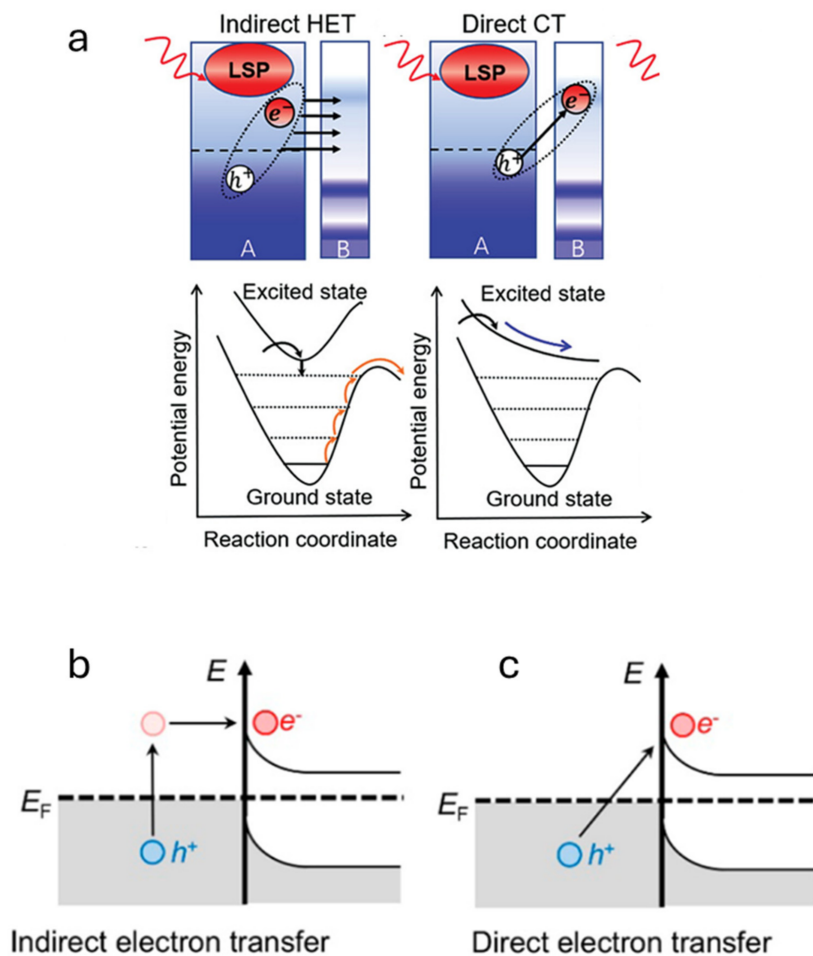


Figure 6. (a) Indirect and direct charge transfer mechanisms (HET—hot electron transfer; CT—charge transfer). A: metal, B: adsorbate. Figure modified from [49] (Creative Commons CC BY). (b) Indirect

electron transfer and (c) direct electron transfer in a metal/semiconductor interface. Figures modified with permission from [46].

5. Photo-Thermal Dry Reforming of Methane

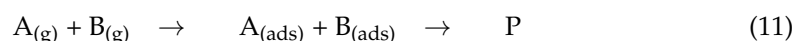
Solar-driven photo-thermal dry reforming of methane is considered among the most promising processes to convert GHGs into valuable chemicals. However, it suffers from some drawbacks that currently limit its application at the industrial scale, such as the high cost of electricity, the carbon tax, the limited number of hours during which natural sunlight is used to meet the energetic requirements of the reaction, the cost of the photo-catalyst and the catalyst lifetime [52–55]. Considering these issues [48], the requirements to obtain an efficient PTC-DRM are:

- high visible light absorption;
- good match between the band structure of the catalyst and the redox potentials of the reaction;
- good thermocatalytic activity.

In Figure 7, the description of a proposed simplified PTC-DRM mechanism is presented in which the principal steps are shown. Methane is dissociated by the active metal of the catalyst into CH_x and H^* species, and H^* species combine to produce H_2 (Figure 7a). CO_2 is activated by spillover on the catalyst's surface (Figure 7b) and reacts with H^* and CH^* species to produce CO molecules and to release H_2O , respectively. Methane activation is promoted by holes, and electrons promote the cleavage of the C-O bond in carbon dioxide.

In the literature, two main PTC mechanisms are proposed: monofunctional and bifunctional. It is hypothesized that in the monofunctional PTC mechanism, methane and carbon dioxide are activated on metal sites, following the typical Langmuir–Hinshelwood–Hougen–Watson mechanism; instead, in the bifunctional PTC mechanism, methane is activated on the metal sites and carbon dioxide on the surface of the support [56,57].

According to Langmuir–Hinshelwood–Hougen–Watson mechanism, in a bimolecular reaction such as DRM, three elementary steps are considered. The first one is the adsorption of the gases ($\text{A}_{(g)}$ and $\text{B}_{(g)}$) on adjacent sites, the second step is the reaction of molecules at the surface of the support and the third one is the desorption of the products (11):



Light irradiation enhances, as heat, every step of the PTC mechanism, with the main differences that, compared to dark conditions, methane dissociation is faster [58].

In the study reported by Liu et al. [27], a catalyst with magnesium/aluminum-layered double hydroxides (Mg/Al-LDH) was used with Ni and Co alloys as active species. After light irradiation, methane decomposes into CH_x and H^* species, and in a second step, C^* and H^* species are obtained before the desorption of the products. The activation energy required by using NiCo alloy was higher compared to that for catalysts employing only Ni or Co as active metals, to prevent the formation of carbon on the surface of the catalyst. This is one of the most accepted pathways for the DRM reaction; low activation energies of CH^* oxidation compared to the oxidation of C^* to CO^* disfavor the deposition of carbon on the surface of catalysts.

Going deep into the DRM reaction, the value of the GHSV (Gas Hourly Space Velocity), i.e., the volume of a gas entering a reactor per hour per unit volume of catalyst, must also be considered. GHSV is calculated by the following Equation (12):

$$\text{GHSV} = [\text{F}_{\text{tot}} \cdot 3600 \cdot (\text{s} \cdot \text{h}^{-1})] / (\text{V}_{\text{cat}}) \quad (12)$$

where F_{tot} is the total flow rate used in the experiment and V_{cat} is the volume of the catalyst. GHSV is expressed as h^{-1} . The inverse of this value is the space time τ (13), which represents the residence time of the gasses with catalyst:

$$\tau = \text{GHSV}^{-1} \quad (13)$$

The yield of the DRM reaction increases by increasing the residence time (decreasing the GHSV) due to the higher number of adsorbed reactants on the catalytic surface.

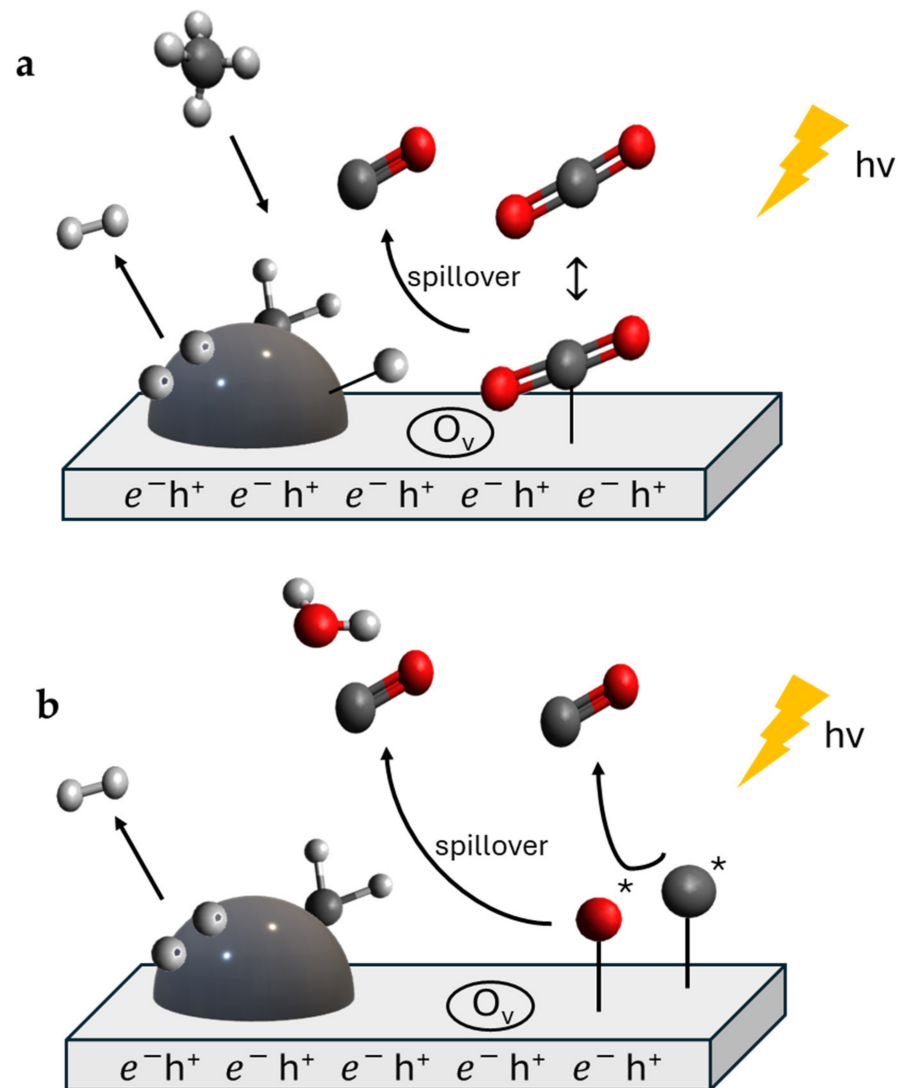


Figure 7. Simplified mechanism of PTC-DRM. (a) Activation of methane; (b) activation of carbon dioxide. The symbol $*$ indicates the species adsorbed on the surface of the catalyst. O_v stands for oxygen vacancy.

PTC is performed, usually, in a fixed bed reactor or in a stainless-steel reactor in which the catalyst is contained in a quartz tube to guarantee homogeneous heating. After the introduction of the sample into the reactor, the feed ratio of the gases is fixed at a certain temperature and the catalyst, if necessary, is reduced by hydrogen.

A simplified scheme of a type of reactor for PTC-DRM is presented in Figure 8.

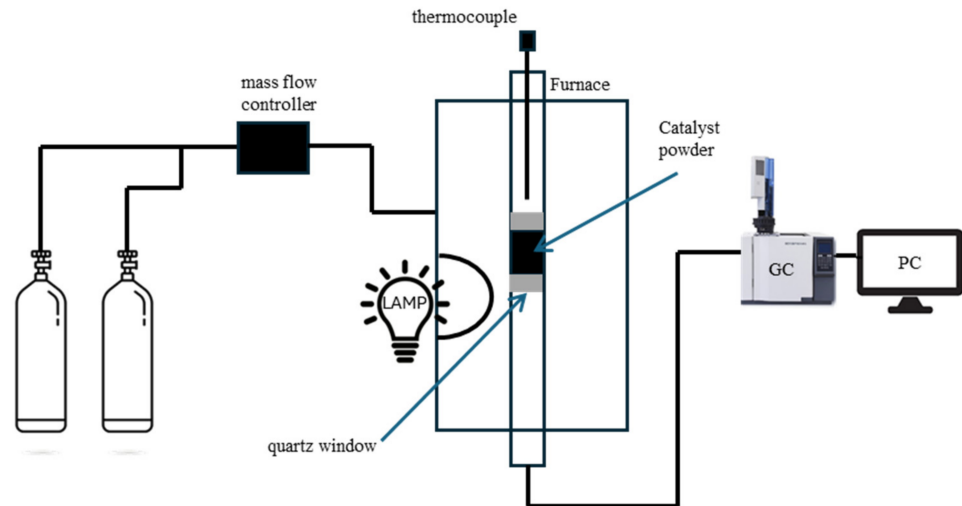


Figure 8. Exemplified scheme of a fixed bed reactor for PTC-DRM.

In this representation, a reactor containing the catalyst is positioned inside a tubular vertical furnace and a source of light is used to promote the DRM reaction. After conversion, the produced gases are analyzed by a gas analyzer.

When the DRM is carried out at “low” temperatures, i.e., at $T < 600\text{ }^{\circ}\text{C}$, the yields of the products are low and, in addition, at temperatures lower than $325\text{ }^{\circ}\text{C}$, the disproportionation of carbon dioxide is favored. Disproportionation of CO_2 produces different types of carbon species, which cause the deactivation of the catalysts [21,59]. On the other hand, starting from $T > 650\text{ }^{\circ}\text{C}$, methane cracking is favored, especially on Ni-based catalysts. The formation of solid carbon $\text{C}_{(s)}$ during CO_2 reforming of CH_4 may therefore occur either via CH_4 cracking (14) or CO disproportionation (i.e., the Boudouard Reaction (15)) [24]:

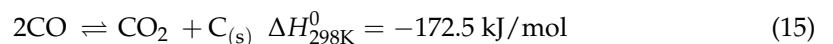
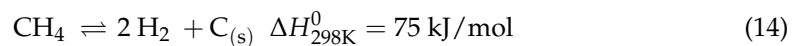


Figure 9 illustrates the formation of a coke deposit on a catalyst surface. It is evident how carbon deposits hinder the catalytic activity, blocking the active sites, which cannot be used by active metals [59].

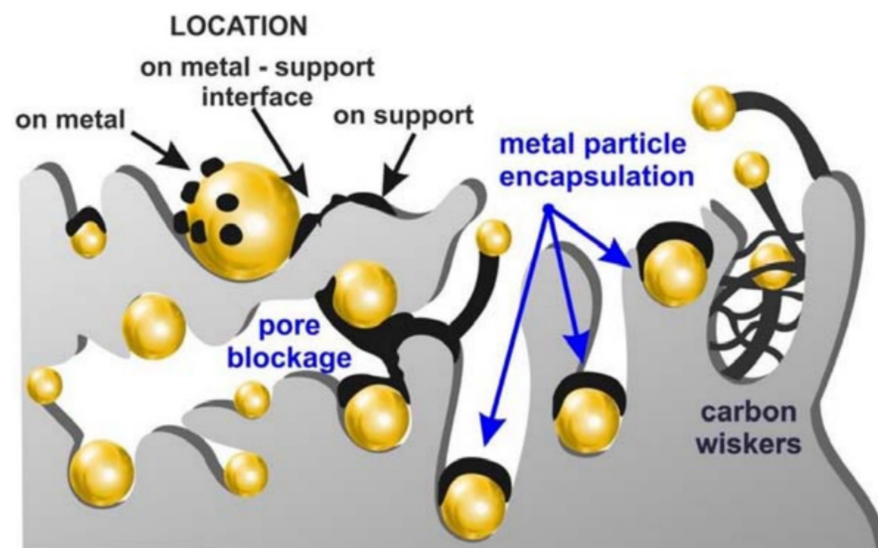


Figure 9. Formation of a coke deposit on a surface of a catalyst. Reprinted from [60]. Copyright MDPI 2021.

Another crucial point is to understand how the carbon, derived from CO₂ and CH₄ adsorption, affects the lowering of the activation energies of the elementary steps [23]. In a recent review from Xu and Park [59], the main deactivation mechanisms of Ni-based catalysts are discussed, together with strategies to limit coke formation to improve the catalysts' performance and stability.

6. Catalysts for PTC-DRM Reaction

In this last section, catalysts for the DRM reaction have been divided into two main classes: PGM-based and PGM-free catalysts, according to the active metal components.

As already said, PGM stands for Platinum Group Metal, i.e., platinum, palladium, rhodium, ruthenium, iridium and osmium. These metals have high catalytic activity due to their high heat and corrosion resistance, which make them almost unique for a vast range of industrial, medical and electronic applications. However, PGMs are listed among the critical raw materials (CRMs) for the EU [61], and many efforts are being devoted to their recovery from end-of-life products or to their partial or total substitution. It is worth noting that the support also plays a fundamental role in determining catalysts' overall performance, because the support can provide additional catalytic sites, good dispersion of the active metal, increased surface area, etc., and the interaction between the support and the active component is fundamental in determining the catalytic activity and the selectivity of the catalysts [62].

6.1. PGM-Free Catalysts

The PGM-free catalysts for DRM are mostly based on Ni or Co as monometallic or bimetallic active compounds dispersed on different types of supports, mainly oxides [63–66]. It is worth noting that Ni was recently added to the CRM list, while Co, which has been on the CRM list since 2011, presents additional cancerogenic issues [67]. Ni and Co cost is, however, much lower than that of PGMs [68].

In a recent study, Hu et al. [69] synthesized a catalyst for PTC-DRM containing Ni supported on Al₂O₃, which showed 142.8 and 160.2 mmol g_{Ni}⁻¹ h⁻¹ yields of H₂ and CO, respectively. Photo-thermal conditions helped in the formation of Ni⁽⁰⁾ and in obtaining hydrogen molecules starting from methane. However, catalysts supported on acidic materials, such as alumina, rapidly deactivate due to coke deposition, and this is one of the reasons why supports like CaO are often used [57]. In fact, CaO is a promising support for the DRM reaction, because of its high coke resistance, good dispersion of metal and strong metal–support interaction. Moreover, it is cheap, easily available, non-corrosive and environmentally friendly [70]. CaO is used to provide basic sites for the adsorption of CO₂, but rarely, CaO is used alone, because it reacts with CO₂ to form CaCO₃. This is the reason why CaO is generally combined with other oxides to enhance the catalytic activity. ZrO₂ is used with CaO to increase the activity of the catalyst, and it exhibits a strong metal–support interaction and stabilizes oxygen vacancies in the ZrO_x lattice. A very recent study on the modification of CaO-based adsorbents and Ni-based catalysts for DRM and CaL (calcium looping) was recently reported by Wang et al. [71]. Even SiO₂ is an excellent choice because of its inertness, its low cost and low toxicity [72].

A catalyst with (Ni/CeO₂)-SiO₂ was demonstrated to be a useful obstacle to carbon deposition and sintering, due to its silica shell. From the Scherrer equation, the Ni sizes were 3.5 nm in the catalyst submitted to the DRM test. These values were close to the ones for the reduced catalyst, confirming the non-occurrence of Ni sintering. These findings were also confirmed by TEM images. Despite the fact that carbon deposition was confirmed by TGA analysis, its amount was very low, about 0.5% of the total amount of catalyst. The loss of carbon occurred in the temperature range of 800–1073 K and the reduction of nickel ion to metal was confirmed by XPS analysis. The fast CO₂ activation was attributed to the reduction of Ce⁴⁺ to Ce³⁺, which led to a higher number of oxygen vacancies [73].

The creation of oxygen vacancies can be explained easily using cerium oxide as an example. Ce⁴⁺ leads to a re-distribution of the charge during the reduction of the ions;

when CO₂ molecules interact with the surface, the electronic density increases, CO₂ accepts an electron and the adjacent oxygen vacancy acts as a sink to detach and accommodate the oxygen anion, replenishing the vacancy. At the end, the CO₂ energy activation barrier for the breaking of the bond between C and O is reduced [55,74–76].

Perovskites are being extensively investigated for the DRM reaction and have been demonstrated to have high activity, even though challenges still exist for their application at the industrial scale due to carbon deposition and thermal stability. Perovskites are based on the general formula ABO₃/A₂BO₄, where A is usually a rare earth, alkaline earth or alkali metal ion, and B is a transition metal cation. The catalytic properties of perovskites are significantly affected by the choice of A and B metal cations, by the preparation techniques and by the partial substitution of A and B cations. A recent review paper on dry reforming of methane over perovskite-derived catalysts is reported in [77]. As oxides, perovskites can handle high-temperature processes [57,78]. The insertion of calcium in a perovskite structure can improve oxygen storage capacity by creating oxygen defects, leading to a relatively high surface-to-volume ratio.

To study oxygen vacancies, two important techniques can be used: Electron Paramagnetic Resonance (EPR), in which, at a g value (specific value calculated for this technique) of 2.004, a high density of oxygen vacancies in the catalyst is evidenced, and X-ray Photoelectron Spectroscopy (XPS), by analyzing the O 1s region, where the three peaks around 530 eV can be attributed to oxygen lattice, vacancies and adsorbates. The oxygen vacancy-to-lattice oxygen ratio gives insights into the diffusion during the charge transfer [79–81].

Bimetallic alloys are very effective in enhancing the performances of the catalysts during heterogeneous catalysis. Zhang et al. [26] synthesized NiCo alloys on SiO₂ supports and observed that CO₂ conversion increased when light changed from high to low wavelengths, i.e., at higher energy. In their study, Field Emission Microscopy (FEM) was very useful to understand the role of hot carriers in PTC. 1.2 Ni_{0.3}Co/SiO₂ showed the highest values of quantum efficiency (Equation (9)) of 67 and 58% at 420 and 500 nm, respectively.

Takami et al. achieved conversion rates of 21% for CO₂ and 20% for CH₄ even at 473 K in a DRM reaction under visible light with a plasmonic Ni/Al₂O₃ photocatalyst. The production rates of CO and H₂ were 1.87 and 1.20 mmol h^{−1}, respectively [82].

Production rate can be calculated using (15) [51]:

$$r_i = (C_{outlet} \times V_{outlet} \times 60) / (22.4 \times m_{cat}) \quad (16)$$

where C_{outlet} and V_{outlet} are, respectively, concentration and volume of the gas, m_{cat} is the mass of the catalyst and r_i is the outlet from the reactor.

In [28], Xie et al. compared three different experimental conditions, thermo-, photo- and photo-thermal, and used TiO₂ as support, which is commonly used for photothermal catalysts. In their study, the authors reported how the synergistic effect of light and heat improves the formation rates of the products and the conversions of CO₂ and CH₄, mostly due to the separation of the excited electron/hole pairs.

Doping with alkaline metals or their oxide can increase the activity of catalysts due to their abilities to enhance the adsorption and activation of CO₂ molecules. From the Arrhenius plot, apparent activation energy is reduced, passing from 57.2 kJ/mol under dark conditions to 29.5 kJ/mol under light conditions.

Fertout et al. [83] developed Ni catalysts on γ alumina doped with La₂O₃ and alkaline earth oxides (MgO, CaO and SrO), and they promoted the formation of carbonates, instead of hydroxides on these modified supports. Catalytic activity increased with the basicity of metals: Mg < Ca < Sr, probably because of a faster activation of CO₂. Strontium has strong basicity, but magnesium improves the dispersion of Ni by surface rearrangement and calcium enhances the thermal stability and suppresses carbon deposition, even though it decreases the catalytic activity.

Khan et Tahir [84] developed TiO₂ NP-embedded 2D Ti₃C₂ exfoliated sheets coupled with g-C₃N₄ to construct a 2D/2D g-C₃N₄/Ti₃C₂ heterojunction. The performance of the semiconductor was examined to analyze CO and H₂ production under visible light. The

graphitic carbon nitride (g-C₃N₄) after irradiation with an artificial light source acted as an electron donor. CO decomposition of methane was achieved by electrons donated by methane; holes, CH_x species and H⁺ ions reacted with methane to form a H₂ molecule.

Tahir et al. [85] used g-C₃N₄ combined with Cu and observed that an increase in the amount of copper led to an increase of yields of the products. It is obvious from this study that the introduction of copper in the structure of graphitic carbon nitride is the key to obtain a H₂/CO ratio close to unity. The catalyst's structure was successful in promoting the DRM reaction because Cu/g-C₃N₄ decreased the CO selectivity due to a more prolific production of electrons.

Table 1 reports the DRM performances of PGM-free catalysts on several types of supports. In Table 2, the performances of catalysts exposed to an external source of light are reported.

Table 1. Gas hourly space velocity of state-of-the-art DRM catalysts at different temperatures and feed ratio CH₄/CO₂ equal to 1/1.

Catalysts	GHSV h ⁻¹	τ s	Temperature °C	Catalytic Performances	References
CeO ₂ -Ni/CaO-Al ₂ O ₃	9000	0.4	700	CH ₄ conv. = 81% CO ₂ conv. = 84%	[81]
Sm/Ni/Al ₂ O ₃ -CaO	12,000	0.3	700	CH ₄ conv. = 68% CO ₂ conv. = 43% H ₂ /CO = 0.64	[86]
7%Ni/CaO-Al ₂ O ₃	1800	0.5	700	CH ₄ conv. = 66% CO ₂ conv. = 62% H ₂ /CO = 0.85	[87]
Ni-CaO-ZrO ₂	48,000	0.075	750	CH ₄ conv. = 82% H ₂ /CO = 0.94	[88]
CaZr _{0.8} Ni _{0.2} O _{3-δ}	28,800	0.125	800	CH ₄ conv. = 95% CO ₂ conv. = 96% H ₂ /CO = 0.98	[89]

Table 2. Catalytic performances of PGM-free catalysts. Production rates have been calculated using (16). For solar irradiation, a Xe lamp was used. Feed ratio of CH₄/CO₂ is 1/1.

Catalyst	Surface Temperature °C	Light Intensity mW·cm ⁻²	Catalytic Performances	Reference
CN/TNT	25	20	r (H ₂) = 49 μmol·g ⁻¹ ·h ⁻¹ r (CO) = 75 μmol·g ⁻¹ ·h ⁻¹ H ₂ /CO = 0.64	[84]
(Ni/CeO ₂)-SiO ₂	750	-	CH ₄ conv. = 66% CO ₂ conv. = 80% H ₂ /CO = 0.90	[73]
Ni ₃ Fe ₁ nanoalloy	350	3.62	r (H ₂) = 326 × 10 ³ μmol·g ⁻¹ ·h ⁻¹ r (CO) = 632 × 10 ³ μmol·g ⁻¹ ·h ⁻¹ H ₂ /CO = 0.52	[90]
La/TiO ₂	100	150	r(H ₂) = 74 μmol·h ⁻¹ ·g _{cat} ⁻¹ r (CO) = 183 μmol·h ⁻¹ ·g _{cat} ⁻¹ H ₂ /CO = 0.40	[91]

Table 2. Cont.

Catalyst	Surface Temperature °C	Light Intensity mW·cm ⁻²	Catalytic Performances	Reference
Cu-g-C ₃ N ₄	100	100	r(H ₂) = 76 μmol·h ⁻¹ ·g _{cat} ⁻¹ r(CO) = 142 μmol·h ⁻¹ ·g _{cat} ⁻¹ H ₂ /CO = 0.54	[85]
Ni/Ga ₂ O ₃	391	1.9–3	r (H ₂) = 194 μmol·g ⁻¹ ·h ⁻¹ r (CO) = 206 μmol·g ⁻¹ ·h ⁻¹ H ₂ /CO = 0.94	[92]

To better compare the different types of catalysts, the turnover frequency (T.O.F.) should also be considered. In [93], T.O.F. is expressed by two different Equations (17) and (18):

$$\text{T.O.F.} = \text{specific rate (converted molecules} \cdot \text{s}^{-1} \cdot \text{g}^{-1}) / L \text{ (active sites} \cdot \text{g}^{-1}) \quad (17)$$

$$\text{T.O.F.} = \text{areal site (converted molecules} \cdot \text{s}^{-1} \cdot \text{nm}^{-2}) / d_s \text{ (active sites} \cdot \text{nm}^{-2}) \quad (18)$$

Specific rate refers to converted molecules per second per mass of sample. L is expressed as active sites per mass of sample and d_s is expressed as active sites per surface area of sample (19).

$$L = d_s \left(\text{active sites} / \text{nm}^2 \right) \times A \left(\text{nm}^2 / \text{g} \right) \quad (19)$$

where d_s is the surface density of active sites and A is the surface area of the catalyst.

The difficulty in calculating T.O.F. lies in the exact determination of active sites, which is why the definition of T.O.F. is still debated [94].

If T.O.F. increases, the conversions of reactants also increase, and this means that photo-thermal conditions are more efficient than thermal conditions. As an example, in [73], it was found that at the same temperature of 750 °C, in the presence of (Ni/CeO₂)-SiO₂ catalyst, the conversions of CO₂ and CH₄ using the photo-thermal approach were 42.8 and 19%, respectively, while using only the thermal approach, conversion rates were much lower, i.e., 10.5 and 6.4 for carbon dioxide and methane, respectively.

In the case of a structure-insensitive reaction, T.O.F. is constant. If the catalytic reaction is structure-sensitive, T.O.F. depends on the size of the catalyst particles [95].

In the work from Vogt et al. [96], the catalyst is formed by different-sized Ni nanoparticles on a SiO₂ support to prevent the formation of carbon on its surface. By changing the morphology of the catalyst, two different conditions for SRM and DRM are found. In the first one, T.O.F. increases with the increase in Ni particle size. The explanation is that bonds are cleaved preferentially over highly under-coordinated atoms in the metal nanoparticles. A change in the morphology of the sample will contribute to a change in the value of T.O.F., which depends directly on the rate-determining step, and this is also related to the intermediates involved during the DRM reaction. As an example, FTIR experiments evidenced that there are peaks attributed to the presence of CO molecules adsorbed in two different positions, top and bridge, and the ratio of the two peaks corresponding to CO_{ads-top} and CO_{ads-bridge} is correlated with the T.O.F. trend.

In Table 3 the effect of different supports on Ni-based catalysts is reported.

Table 3. Characteristics of Ni-based catalysts with different supports and coatings: turnover frequencies and conversion of methane and carbon dioxide. Feed ratio of CH₄/CO₂ is 1/1.

Samples	Temperature °C	T.O.F. (CH ₄) s ⁻¹	T.O.F. (CO ₂) s ⁻¹	CH ₄ conv %	CO ₂ conv %	References
Ni/SiO ₂ @Al ₂ O ₃	800	135.2	177.2	62.8	82.3	[97]
Ni/SiO ₂ @MgO	800	120.0	171.1	50.0	71.3	[97]
Ni/SiO ₂ @ZrO ₂	800	29.5	37.8	29.1	37.3	[97]
Ni/SiO ₂ @TiO ₂	800	12.9	18.1	17.0	23.8	[97]
Ni-Zr/SiO ₂	400	0.32	0.32	2	2	[98]
Ni-Zr/SiO ₂	450	1.06	1.48	0.8	1.2	[98]
Ni-Si/ZrO ₂	400	0.50	0.44	4.3	3.8	[98]
Ni-Si/ZrO ₂	450	1.38	1.30	1.6	2.4	[98]

6.2. PGM-Based Catalysts for Photo-Thermal DRM

In this section, performances of catalysts containing Platinum Group Metals as active metals for PTC-DRM will be discussed. These precious metals can improve radically the catalytic activity of the DRM reaction, and they have a strong resistance to carbon deposition [19,99].

However, as already mentioned, also for these catalysts the support plays a fundamental role in the photocatalytic response, as we can see in the next two examples.

Yao et al. [74] developed a highly efficient photothermal Rh/LaNiO₃ catalyst for solar-driven DRM, obtaining high generation rates for H₂ and CO of 452.3 and 527.26 mmol·g_{Rh}⁻¹·h⁻¹, respectively, under the irradiation of a 300 W Xe lamp of 1.5 W/cm², without external heating.

In a previous work from the same group, Yang et al. [100] developed an all-in-one photothermal and photoelectric catalytic DRM process employing a Rh/Ce_xWO₃ catalyst. Also, in this case, the experiment was carried out under irradiation of a Xe lamp without external heating. For 1.8 W/cm² irradiation, the generation rates of H₂ and CO were 88.5 and 152.3 mmol·g_{Rh}⁻¹·h⁻¹, respectively.

In both studies, Rh was uniformly dispersed on the oxide supports and E_{act} (H₂) and E_{act} (CO) were 43.89 and 39.99 kJ/mol for Rh/Ce_xWO₃ and 115.3 and 87.5 kJ/mol for Rh/LaNiO₃ catalyst, respectively. In both situations, Rh provided a low electronic density and this led to the promotion of breaking of methane bonds and to the formation of H₂. The formation of oxo-bridges lowered the start-up temperature of the DRM reaction, the temperature at which the reaction becomes spontaneous, according to Equation (2). In both studies, a migration of oxygen was reported, from Ce to W in the Rh/Ce_xWO₃ catalyst, and from La to Ni in the Rh/LaNiO₃ catalyst. The weaker the binding in the oxo-bridge, the higher the migration of oxygen atoms. This is the main reason why E_{act} was lower in the case that Ce_xWO₃ was used as a support. The higher production rates obtained in the case of a catalyst with LaNiO₃ support were attributed to the high number of oxygen defects able to effectively activate CO₂ and enhance the interaction between the support and the Rh nanoparticles.

Yin and coworkers [101], who used a catalyst made of Ru and Ni alloys on an Al₂O₃ support, obtained very high values of production rates of H₂ and CO: 539 and 642 mmol·g⁻¹·h⁻¹, respectively. In their work, the light irradiation and the thermal decomposition of carbonates are used to promote the DRM reaction. Methane reacts with CO₂ produced by thermal decomposition of MgCO₃, producing MgO and syngas. MgCO₃ decomposes completely into MgO at 400 °C in 5% CH₄/Ar, as evident from the XRD analysis. Generation rates of H₂ and CO increase during the first 20 min up to 0.68 and 0.44 mmol·g⁻¹·h⁻¹, respectively, and selectivity of carbon dioxide decreases by 20% after one hour with the consumption of MgCO₃. The increase in generation rates is due

to the formation of carbonates, external light irradiation and localized surface plasmon resonance effect.

Song et al. [102], who used a Pt-Au/SiO₂ catalyst (Pt content= 0.5–1.5 wt.%), obtained H₂ and CO generation rates of, respectively, 5.5 and 7.2 mmol·g⁻¹·h⁻¹ at 400 °C using a light intensity of 0.6 μW·cm⁻². This catalyst presents a high surface area of 436 m²/g and the aggregate structure made of Pt and Au is thermodynamically stable. The temperature is comparable to the one used for the case of Yin et al. [101], but there is a huge difference in the value of light intensity used in these two studies. In the study of Yin, in fact, the intensity of light (13.5 W/cm²) is much higher than that used in the study of Song (0.6 μW/cm²). This explains the difference in the values of generation rates of products.

In all of the above-mentioned studies, SEM analysis has evidenced that catalytic metals are well dispersed on each support and no agglomeration is found on the surface of the catalysts used.

One of the most used supports to perform PTC-DRM is anatase TiO₂ due to its narrow band gap, its ability to suppress carbon deposition and its good redox properties for oxygen mobility [99].

Zhang et al. [58] have investigated the performances of a Pt/mesoporous-TiO₂ catalyst under different experimental conditions: reaction temperature, intensity of light and CO₂/CH₄ molar ratio. Authors found that a moderate increase in CO₂ partial pressure was beneficial to the further dissociation of CH₄, while the total amount of dissociated H species diminished with CO₂/CH₄ greater than 1.08/1. For CO formation, the authors proposed two possible pathways; the first one consists of the decomposition of HCOO⁻ and the second one consists of the dissociation of the CO₂ molecule.

Wu et al. [103] reported two different situations for Pt nanocrystals partially confined in mesoporous CeO₂ nanorods (Pt/CeO₂-MNR). In the first one, under focused UV-Vis-IR illumination, r (H₂) and r (CO) were, respectively, 5.7 and 6.0 mmol g⁻¹ min⁻¹, while under visible-IR illumination, r (H₂) and r (CO) were 4.9 and 5.2 mmol g⁻¹ min⁻¹, respectively. In the latter case, authors found an improved photoactivation which inhibits CO disproportionation as a major side reaction of coke formation, promoting the oxidation of carbon species produced by CH₄ dissociation and thus increasing the H₂/CO ratio.

Another study shows the effect of the structure of the support [104]. In this work, Pt is combined with two different supports, i.e., a mesoporous TiO₂ and P25. Higher production rates are obtained in the first case because of the mesoporous structure, which shows a different light absorption response, a different recombination of electrons and holes and a narrower band gap. This explains why at the same temperature of 500 °C and at the same intensity of light of 4.76 W/cm², the production rates of H₂ and CO are 178.6 and 281 mmol·g_{Pt}⁻¹·h⁻¹ and 39.8 and 105.6 mmol·g_{Pt}⁻¹·h⁻¹ in the case of mesoporous titania and P25, respectively.

In the study from Zhang et al. [105], the photo-thermal properties of a Pt-Au/P25 composite catalyst have been enhanced with the LSPR effect. The authors found that plasmonic nanoparticles act as electron traps, inhibiting the recombination of electron–hole pairs and promoting the PTC-DRM reaction. In the case of Pt and Au, their behavior was identical due to their similar atomic number. Even if Pt-Au/P25 had the smallest value of surface area, the catalyst had a good catalytic activity due to the Fermi energy levels of both metals, which helped to lower the valence band (2.67 eV). This led to an increase in generation rates, which increased linearly with the light intensity increase, and to the promotion of a better migration of holes. In this study the Pt-Au/P25 catalyst had a strong metal–surface interaction, and no deactivation during a 10 h DRM test was observed. The DRM results show how light can improve yields of products, 85.38 and 201.92 mmol·g_{Pt}⁻¹·h⁻¹ for H₂ and CO, respectively, favoring the dissociation of methane and CO₂, while lower values were obtained in the case that only heat was used, 27.60 mmol·g_{Pt}⁻¹·h⁻¹ for H₂ and 97 mmol·g_{Pt}⁻¹·h⁻¹ for CO.

Platinum is a very efficient catalytic metal for the DRM reaction [32,80,106,107]. The DRM reaction can be better performed on the active sites of precious metals due to their

higher electron cloud density being able to reinforce the redox reactions on the surface of the catalysts. By combining precious metals and metals such as nickel and cobalt, high yields of products can be achieved [64]. It can be noted that the sample “0.3 Ni”, reported in Table 4, has the highest value of BET surface area but deactivates very rapidly when compared to the other catalysts. Comparison of 0.2, 0.3 and 0.4 PdNi bimetallic catalysts shows that increasing the amount of Pd, two situations arise:

- the dispersion of Ni decreases;
- sintering becomes more significant, and this leads, inevitably, to a decrease in the BET surface area.

Table 4. BET results on different catalysts. Feed ratio of CH₄/CO₂ is 1/1.

Name Sample	Temperature °C	Light Intensity W/cm ²	BET Surface Area m ² /g	Pore Volume cm ³ /g	Average Pore Diameter nm	Catalytic Performances	References
P25	500	4.6	63.0	0.12	7.9	N.A.	[105]
Pt/P25	500	4.6	62.0	0.14	9.1	r (H ₂) = 65 mmol·g ⁻¹ ·h ⁻¹ r (CO) = 162 mmol·g ⁻¹ ·h ⁻¹ H ₂ /CO = 0.40	[105]
Au/P25	500	4.6	60.0	0.14	9.3	N.A.	[105]
Pt-Au/P25	500	4.6	55.0	0.12	8.7	r (H ₂) = 86 mmol·g ⁻¹ ·h ⁻¹ r (CO) = 203 mmol·g ⁻¹ ·h ⁻¹ H ₂ /CO = 0.42	[105]
mes-TiO ₂	500	3.8	91.8	0.25	10.7	N.A.	[104]
P25	500	3.8	62.0	0.12	7.5	N.A.	[104]
Pt/P25	500	3.8	54.3	0.11	8.4	r (H ₂) = 40 mmol·g ⁻¹ ·h ⁻¹ r (CO) = 106 mmol·g ⁻¹ ·h ⁻¹ H ₂ /CO = 0.38	[104]
Ni/mes-TiO ₂	500	3.8	85.1	0.24	11.1	r (H ₂) = 31 mmol·g ⁻¹ ·h ⁻¹ r (CO) = 81 mmol·g ⁻¹ ·h ⁻¹ H ₂ /CO = 0.38	[104]
Pt/mes-TiO ₂	500	3.8	77.5	0.22	11.4	r (H ₂) = 211 mmol·g ⁻¹ ·h ⁻¹ r (CO) = 309 mmol·g ⁻¹ ·h ⁻¹ H ₂ /CO = 0.68	[104]
0.3 Ni	650	0	580.7	0.39	2.2	CH ₄ = 16% CO ₂ = 25% H ₂ /CO = 0.69	[64]
0.2 PdNi	650	0	523.6	0.38	2.4	CH ₄ = 23% CO ₂ = 31% H ₂ /CO = 0.83	[64]
0.3 PdNi	650	0	514.7	0.35	2.2	CH ₄ = 36% CO ₂ = 52% H ₂ /CO = 0.81	[64]
0.4 PdNi	650	0	506.6	0.35	2.1	CH ₄ = 30% CO ₂ = 42% H ₂ /CO = 0.81	[64]
Ni/CaO-Al ₂ O ₃	700	0	76.1	0.21	11.1	CH ₄ conv. = 54% CO ₂ conv. = 59%	[81]
CeO ₂ -Ni/CaO-Al ₂ O ₃	700	0	90.7	0.29	13.2	CH ₄ conv. = 82% CO ₂ conv. = 84%	[81]

High surface area leads to a higher contact area for the reactants, leading to a higher activity. These last two examples underline the importance of the interaction between support and metal, as mentioned before, and it is evident in the two cases of Ni/CaO-Al₂O₃ and CeO₂-Ni/CaO-Al₂O₃ that high surface areas resulted in high dispersion of Ni on the support, thus increasing the catalytic activity [81].

Moreover, as occurs in the case of PGM-free catalysts, an appropriate choice of support, doping and active metal is needed. On the one hand, in fact, doping of the support can induce localized states in the band gap, which may increase the absorption ability of the photocatalyst, but on the other hand, localized band states may increase the charge carrier recombination, decreasing the catalytic activity.

Table 5 reports the catalytic performances under different conditions for PGM-based catalysts.

Table 5. Catalytic performances of PGM-based catalysts for photo-thermal dry reforming of methane under different working conditions. Xe lamp was used, except for [55], in which concentrated sunlight was used. Feed ratio of CH₄/CO₂ is 1/1.

Catalyst	Surface Temperature °C	Light Intensity W·cm ⁻²	Catalytic Performances	Reference
Rh/La ₂ O ₃	340	1.5	r (H ₂) = 452 mmol·g ⁻¹ ·h ⁻¹ r (CO) = 527 mmol·g ⁻¹ ·h ⁻¹ H ₂ /CO = 0.86	[74]
Pt/TiO ₂	500	4.67	r (H ₂) = 134 mmol·g ⁻¹ ·h ⁻¹ r (CO) = 221 mmol·g ⁻¹ ·h ⁻¹ H ₂ /CO = 0.61	[58]
Pt/TiO ₂	350	4.67	r (H ₂) = 7 mmol·g ⁻¹ ·h ⁻¹ r (CO) = 22 mmol·g ⁻¹ ·h ⁻¹ H ₂ /CO = 0.32	[58]
Pt/TiO ₂	500	3.72	r (H ₂) = 121 mmol·g ⁻¹ ·h ⁻¹ r (CO) = 200 mmol·g ⁻¹ ·h ⁻¹ H ₂ /CO = 0.61	[58]
MgO/Pt/Zn-CeO ₂	600	3	r (H ₂) = 356 mmol·g ⁻¹ ·h ⁻¹ r (CO) = 516 mmol·g ⁻¹ ·h ⁻¹ H ₂ /CO = 0.69	[55]
Ru-Al/LDH	350	13.5	r (H ₂) = 9 mmol·g ⁻¹ ·h ⁻¹ r (CO) = 11 mmol·g ⁻¹ ·h ⁻¹ H ₂ /CO = 0.76	[101]
Pt/TiO ₂	500	0.4	r (H ₂) = 598 mmol·g ⁻¹ ·h ⁻¹ r (CO) = 902 mmol·g ⁻¹ ·h ⁻¹ H ₂ /CO = 0.66	[51]
Pt/TiO ₂	700	0.4	r (H ₂) = 1103 mmol·g ⁻¹ ·h ⁻¹ r (CO) = 1495 mmol·g ⁻¹ ·h ⁻¹ H ₂ /CO = 0.74	[51]

Table 5. Cont.

Catalyst	Surface Temperature °C	Light Intensity $W \cdot cm^{-2}$	Catalytic Performances	Reference
Pt/TiO ₂	500	3.76	$r(H_2) = 211 \text{ mmol} \cdot g^{-1} \cdot h^{-1}$ $r(CO) = 309 \text{ mmol} \cdot g^{-1} \cdot h^{-1}$ $H_2/CO = 0.68$	[104]
Pt/TiO ₂	500	2.2	$r(H_2) = 103 \text{ mmol} \cdot g^{-1} \cdot h^{-1}$ $r(CO) = 179 \text{ mmol} \cdot g^{-1} \cdot h^{-1}$ $H_2/CO = 0.58$	[104]

In Table 6, the performance of catalysts for the photo-thermal dry reforming of methane reaction using different values of flow rates of feed gases is presented.

Table 6. Performance comparison of catalysts for photo-thermal dry reforming of methane using different values of flow rates (GHSV). – the value of light intensity is not available.

Catalyst	Temperature °C	Light Intensity $mW \cdot cm^{-2}$	GHSV h^{-1}	Catalytic Performances	References
Ru/SrTiO ₃	600	–	4592	$r(H_2) = 320 \text{ mmol} \cdot g^{-1} \cdot h^{-1}$ $r(CO) = 387 \text{ mmol} \cdot g^{-1} \cdot h^{-1}$ $H_2/CO = 0.83$	[32]
Pt/TiO ₂	500	3.22	40,000	$r(H_2) = 211 \text{ mmol} \cdot g^{-1} \cdot h^{-1}$ $r(CO) = 309 \text{ mmol} \cdot g^{-1} \cdot h^{-1}$ $H_2/CO = 0.68$	[104]
Pt/P25	500	3.22	40,000	$r(H_2) = 40 \text{ mmol} \cdot g^{-1} \cdot h^{-1}$ $r(CO) = 106 \text{ mmol} \cdot g^{-1} \cdot h^{-1}$ $H_2/CO = 0.38$	[104]
Pt/TiO ₂	500	4.67	320,000	$r(H_2) = 55 \text{ mmol} \cdot g^{-1} \cdot h^{-1}$ $r(CO) = 73 \text{ mmol} \cdot g^{-1} \cdot h^{-1}$ $H_2/CO = 0.75$	[58]

7. Conclusions

This paper presents an overview of the current trends in PGM-based and PGM-free catalysts for photo-thermal dry reforming of methane, also highlighting drawbacks for large-scale PTC-DRM applications. With appropriate catalyst design, dry reforming of methane at high temperatures produces a syngas with a high conversion efficiency, generally higher than that obtained in solar-driven DRM reactions. However, if on the one hand, DRM at high temperature does not meet the needs of further industrial applications due to the high costs of materials for the catalysts and reactor, then on the other hand, the limited utilization of visible light limits the scalability of PTC-DRM at the industrial level. The synergistic effect of heat and light irradiation can therefore be a valuable solution to lower the temperature of the DRM process and increase process yields, making PTC-DRM a possible competitive technology for converting greenhouse gases into fuels at a large scale. The yields of the DRM products may, in fact, be enhanced by the photoelectric effect, which leads to a decrease in activation energies under lower-temperature conditions. Supported

precious metal are widely used in DRM; however, several non-precious metals show great potential for reducing DRM costs. A suitable combination of support and catalytic component is a key factor for enhancing the conversion efficiency of the PTC-DRM process; however, issues related to catalyst deactivation due to carbon deposition still need to be completely solved. Coke management is at present one of the main issues limiting the widespread application of DRM technology.

Author Contributions: A.V. and M.L.G. conceived the work. Data curation: A.V., U.P.L., M.F. and M.L.G. Original manuscript writing: A.V. and M.L.G. Review and editing: A.V., U.P.L., M.F. and M.L.G. All authors have read and agreed to the published version of the manuscript.

Funding: This research received no external funding.

Acknowledgments: The following projects: (i) “Chemistry of Platinum Group Metals (CHemPGM)”, H2020-MSCA-RISE-2020 101007669, (ii) Electric System Research Programme, Project 1.6 “Energy Efficiency of Industrial Products and Processes”, Work Package 4 “Production of green H₂ from biomass gasification using efficient CO₂ capture, storage and reuse processes”, financed by the Ministry for the Environment and Energy Security, and (iii) “Development of ECCSEL—R.I. Italian facilities: user access, services and long-term sustainability”, NATIONAL RECOVERY AND RESILIENCE PLAN (PNRR) MISSION 4 “Education and research”, COMPONENT 2 “From research to business”, INVESTMENT 3.1.1 “Fund for the creation of an integrated system of research and innovation infrastructures” (Infrastructures of research), are gratefully acknowledged.

Conflicts of Interest: The authors declare no conflicts of interest.

References

1. Shiraiwa, M. Facing Global Climate and Environmental Change. *ACS Environ. Au* **2023**, *3*, 121–122. [CrossRef] [PubMed]
2. Yoro, K.O.; Daramola, M.O. CO₂ Emission Sources, Greenhouse Gases, and the Global Warming Effect. In *Advances in Carbon Capture: Methods, Technologies and Applications*; Elsevier: Amsterdam, The Netherlands, 2020; pp. 3–28. ISBN 9780128196571.
3. Global Climate Change Impacts in the United States: Highlights—Citations, Rights, Re-Use—UNT Digital Library. Available online: <https://digital.library.unt.edu/ark:/67531/metadc11959/citation/#responsibilities-of-use> (accessed on 4 June 2024).
4. McCulloch, M.T.; Winter, A.; Sherman, C.E.; Trotter, J.A. 300 Years of Sclerosponge Thermometry Shows Global Warming Has Exceeded 1.5 °C. *Nat. Clim. Change* **2024**, *14*, 171–177. [CrossRef]
5. Pearce, J.M.; Parncutt, R. Quantifying Global Greenhouse Gas Emissions in Human Deaths to Guide Energy Policy. *Energies* **2023**, *16*, 6074. [CrossRef]
6. Painter, D.S. Burning Up: A Global History of Fossil Fuel Consumption. *J. Interdiscip. Hist.* **2019**, *50*, 442–443. [CrossRef]
7. Hulme, M. 1.5 °C and climate research after the Paris Agreement. *Nature Clim Change* **2016**, *6*, 222–224. [CrossRef]
8. Parsapur, R.K.; Chatterjee, S.; Huang, K.W. The Insignificant Role of Dry Reforming of Methane in CO₂ emission Relief. *ACS Energy Lett.* **2020**, *5*, 2881–2885. [CrossRef]
9. Li, M.; Sun, Z.; Hu, Y.H. Thermo-Photo Coupled Catalytic CO₂ Reforming of Methane: A Review. *Chem. Eng. J.* **2022**, *428*, 131222. [CrossRef]
10. Ji, G.; Wu, S.; Song, X.; Meng, L.; Jia, Y.; Tian, J. Recent Progress in Photo-Thermal Synergistic Catalysis for Methane Dry Reforming. *Int. J. Hydrogen Energy* **2024**, *57*, 696–708. [CrossRef]
11. Lei, Y.; Ye, J.; García-Antón, J.; Liu, H. Recent Advances in the Built-in Electric-Field-Assisted Photocatalytic Dry Reforming of Methane. *Chin. J. Catal.* **2023**, *53*, 72–101. [CrossRef]
12. Kotkowski, T.; Cherbański, R.; Stankiewicz, A.I. Electrifying the Dry Reforming of Methane. Shall We Target the Chemistry or the Heat Supply? *Chem. Eng. Process.* **2024**, *202*, 109875. [CrossRef]
13. Cho, Y.; Shoji, S.; Yamaguchi, A.; Hoshina, T.; Fujita, T.; Abe, H.; Miyauchi, M. Visible-Light-Driven Dry Reforming of Methane Using a Semiconductor-Supported Catalyst. *Chem. Commun.* **2020**, *56*, 4611–4614. [CrossRef] [PubMed]
14. Jabbour, K. Tuning combined steam and dry reforming of methane for “metgas” production: A thermodynamic approach and state-of-the-art catalysts. *J. Energy* **2020**, *48*, 54–91. [CrossRef]
15. He, Z.; Huang, M.; Lin, T.; Zhong, L. Recent Advances in Dry Reforming of Methane via Photothermocatalysis. *Acta Phys. Chim. Sin.* **2023**, *39*, 2212060. [CrossRef]
16. He, C.; Wu, S.; Wang, L.; Zhang, J. Recent Advances in Photo-Enhanced Dry Reforming of Methane: A Review. *J. Photochem. Photobiol. C* **2022**, *51*, 100468. [CrossRef]
17. Aramouni, N.A.K.; Touma, J.G.; Tarboush, B.A.; Zeaiter, J.; Ahmad, M.N. Catalyst Design for Dry Reforming of Methane: Analysis Review. *Renew. Sustain. Energy Rev.* **2018**, *82*, 2570–2585. [CrossRef]
18. Luyben, W.L. Design and Control of the Dry Methane Reforming Process. *Ind. Eng. Chem. Res.* **2014**, *53*, 14423–14439. [CrossRef]
19. Arora, S.; Prasad, R. An Overview on Dry Reforming of Methane: Strategies to Reduce Carbonaceous Deactivation of Catalysts. *RSC Adv.* **2016**, *6*, 108668–108688. [CrossRef]

20. Wang, S.; Lu, G.Q.; Millar, G.J. Carbon Dioxide Reforming of Methane to Produce Synthesis Gas over Metal-Supported Catalysts: State of the Art. *Energy Fuels* **1996**, *10*, 896–904. [[CrossRef](#)]
21. Pakhare, D.; Spivey, J. A Review of Dry (CO₂) Reforming of Methane over Noble Metal Catalysts. *Chem. Soc. Rev.* **2014**, *43*, 7813–7837. [[CrossRef](#)] [[PubMed](#)]
22. Standard Thermodynamic Quantities for Chemical Substances at 25 °C. In *CRC Handbook of Chemistry and Physics*, 84th ed.; CRC Press: Boca Raton, FL, USA, 2004.
23. Kulandaivalu, T.; Mohamed, A.R.; Ali, K.A.; Mohammadi, M. Photocatalytic Carbon Dioxide Reforming of Methane as an Alternative Approach for Solar Fuel Production—A Review. *Renew. Sustain. Energy Rev.* **2020**, *134*, 110363. [[CrossRef](#)]
24. Bradford, M.C.J.; Vannice, M.A. CO₂ Reforming of CH₄. *Catal. Rev. Sci. Eng.* **1999**, *41*, 1–42. [[CrossRef](#)]
25. Teh, L.P.; Setiabudi, H.D.; Timmiati, S.N.; Aziz, M.A.A.; Annuar, N.H.R.; Ruslan, N.N. Recent Progress in Ceria-Based Catalysts for the Dry Reforming of Methane: A Review. *Chem. Eng. Sci.* **2021**, *242*, 116606. [[CrossRef](#)]
26. Zhang, J.; Xie, K.; Jiang, Y.; Li, M.; Tan, X.; Yang, Y.; Zhao, X.; Wang, L.; Wang, Y.; Wang, X.; et al. Photoinducing Different Mechanisms on a Co-Ni Bimetallic Alloy in Catalytic Dry Reforming of Methane. *ACS Catal.* **2023**, *13*, 10855–10865. [[CrossRef](#)]
27. Liu, X.; Shi, H.; Meng, X.; Sun, C.; Zhang, K.; Gao, L.; Ma, Y.; Mu, Z.; Ling, Y.; Cheng, B.; et al. Solar-Enhanced CO₂ Conversion with CH₄ over Synergetic NiCo Alloy Catalysts with Light-to-Fuel Efficiency of 33.8%. *Sol. RRL* **2021**, *5*, 2100185. [[CrossRef](#)]
28. Xie, T.; Zhang, Z.Y.; Zheng, H.Y.; Xu, K.D.; Hu, Z.; Lei, Y. Enhanced Photothermal Catalytic Performance of Dry Reforming of Methane over Ni/Mesoporous TiO₂ Composite Catalyst. *Chem. Eng. J.* **2022**, *429*, 132507. [[CrossRef](#)]
29. Fang, S.; Hu, Y.H. Thermo-Photo Catalysis: A Whole Greater than the Sum of Its Parts. *Chem. Soc. Rev.* **2022**, *51*, 3609–3647. [[CrossRef](#)] [[PubMed](#)]
30. De Caprariis, B.; De Filippis, P.; Palma, V.; Petrullo, A.; Ricca, A.; Ruocco, C.; Scarsella, M. Rh, Ru and Pt Ternary Perovskites Type Oxides BaZr_(1-x)Me_xO₃ for Methane Dry Reforming. *Appl. Catal. A Gen.* **2016**, *517*, 47–55. [[CrossRef](#)]
31. Rego de Vasconcelos, B.; Pham Minh, D.; Martins, E.; Germeau, A.; Sharrock, P.; Nzihou, A. Highly-Efficient Hydroxyapatite-Supported Nickel Catalysts for Dry Reforming of Methane. *Int. J. Hydrogen Energy* **2020**, *45*, 18502–18518. [[CrossRef](#)]
32. Tang, Y.; Li, Y.; Bao, W.; Yan, W.; Zhang, J.; Huang, Y.; Li, H.; Wang, Z.; Liu, M.; Yu, F. Enhanced Dry Reforming of CO₂ and CH₄ on Photothermal Catalyst Ru/SrTiO₃. *Appl. Catal. B* **2023**, *338*, 123054. [[CrossRef](#)]
33. Sokefun, Y.O.; Trottier, J.; Yung, M.M.; Joseph, B.; Kuhn, J.N. Low Temperature Dry Reforming of Methane Using Ru-Ni-Mg/Ceria-Zirconia Catalysts: Effect of Ru Loading and Reduction Temperature. *Appl. Catal. A Gen.* **2022**, *645*, 118842. [[CrossRef](#)]
34. Fresno, F.; Iglesias-Juez, A.; Coronado, J.M. Photothermal Catalytic CO₂ Conversion: Beyond Catalysis and Photocatalysis. *Top. Curr. Chem.* **2023**, *381*, 21. [[CrossRef](#)] [[PubMed](#)]
35. Ghossoub, M.; Xia, M.; Duchesne, N.P.; Segal, D.; Ozin, G. Principles of photothermal gas-phase heterogeneous CO₂ catalysis. *Energy Environ. Sci.* **2019**, *12*, 1122–1142. [[CrossRef](#)]
36. Entesari, N.; Goepfert, A.; Prakash, G.K.S. Renewable Methanol Synthesis through Single Step Bi-Reforming of Biogas. *Ind. Eng. Chem. Res.* **2020**, *59*, 10542–10551. [[CrossRef](#)]
37. Farooqi, A.S.; Yusuf, M.; Mohd Zabidi, N.A.; Saidur, R.; Sanaullah, K.; Farooqi, A.S.; Khan, A.; Abdullah, B. A Comprehensive Review on Improving the Production of Rich-Hydrogen via Combined Steam and CO₂ Reforming of Methane over Ni-Based Catalysts. *Int. J. Hydrogen Energy* **2021**, *46*, 31024–31040. [[CrossRef](#)]
38. Tahir, M.; Ali Khan, A.; Bafaqeer, A.; Kumar, N.; Siraj, M.; Fatehmulla, A. Highly Stable Photocatalytic Dry and Bi-Reforming of Methane with the Role of a Hole Scavenger for Syngas Production over a Defective Co-Doped g-C₃N₄ Nanotexture. *Catalysts* **2023**, *13*, 1140. [[CrossRef](#)]
39. Lino, A.V.P.; Colmenares Calderon, Y.N.; Mastelaro, V.R.; Assaf, E.M.; Assaf, J.M. Syngas for Fischer-Tropsch Synthesis by Methane Tri-Reforming Using Nickel Supported on MgAl₂O₄ Promoted with Zr, Ce and Ce-Zr. *Appl. Surf. Sci.* **2019**, *481*, 747–760. [[CrossRef](#)]
40. Minh, D.P.; Siang, T.J.; Vo, D.V.N.; Phan, T.S.; Ridart, C.; Nzihou, A.; Grouset, D. Hydrogen Production from Biogas Reforming: An Overview of Steam Reforming, Dry Reforming, Dual Reforming, and Tri-Reforming of Methane. *Hydrog. Supply Chain Des. Deploy. Oper.* **2018**, 111–166. [[CrossRef](#)]
41. Alhassan, M.; Jalil, A.A.; Nabgan, W.; Hamid, M.Y.S.; Bahari, M.B.; Ikram, M. Bibliometric Studies and Impediments to Valorization of Dry Reforming of Methane for Hydrogen Production. *Fuel* **2022**, *328*, 125240. [[CrossRef](#)]
42. Wang, Z.; Yang, Z.; Kadirova, Z.C.; Guo, M.; Fang, R.; He, J.; Yan, Y.; Ran, J. Photothermal Functional Material and Structure for Photothermal Catalytic CO₂ Reduction: Recent Advance, Application and Prospect. *Coord. Chem. Rev.* **2022**, *473*, 214794. [[CrossRef](#)]
43. Linic, S.; Aslam, U.; Boerigter, C.; Morabito, M. Photochemical Transformations on Plasmonic Metal Nanoparticles. *Nat. Mater.* **2015**, *14*, 567–576. [[CrossRef](#)] [[PubMed](#)]
44. Zhang, J.; Chen, H.; Duan, X.; Sun, H.; Wang, S. Photothermal Catalysis: From Fundamentals to Practical Applications. *Mater. Today* **2023**, *68*, 234–253. [[CrossRef](#)]
45. Mateo, D.; Cerrillo, J.L.; Durini, S.; Gascon, J. Fundamentals and Applications of Photo-Thermal Catalysis. *Chem. Soc. Rev.* **2021**, *50*, 2173–2210. [[CrossRef](#)]
46. Zhang, Y.; He, S.; Guo, W.; Hu, Y.; Huang, J.; Mulcahy, J.R.; Wei, W.D. Surface-Plasmon-Driven Hot Electron Photochemistry. *Chem. Rev.* **2018**, *118*, 2927–2954. [[CrossRef](#)] [[PubMed](#)]

47. Song, C.; Wang, Z.; Yin, Z.; Xiao, D.; Ma, D. Principles and Applications of Photothermal Catalysis. *Chem. Catal.* **2022**, *2*, 52–83. [CrossRef]
48. Iglesias-Juez, A.; Fresno, F.; Coronado, J.M.; Highfield, J.; Ruppert, A.M.; Keller, N. Emerging High-Prospect Applications in Photothermal Catalysis. *Curr. Opin. Green. Sustain. Chem.* **2022**, *37*, 100652. [CrossRef]
49. Zhang, Y.; Yan, L.; Guan, M.; Chen, D.; Xu, Z.; Guo, H.; Hu, S.; Zhang, S.; Liu, X.; Guo, Z.; et al. Indirect to Direct Charge Transfer Transition in Plasmon-Enabled CO₂ Photoreduction. *Adv. Sci.* **2022**, *9*, 102978. [CrossRef]
50. Zhu, Z.; Guo, W.; Zhang, Y.; Pan, C.; Xu, J.; Zhu, Y.; Lou, Y. Research Progress on Methane Conversion Coupling Photocatalysis and Thermocatalysis. *Carbon. Energy* **2021**, *3*, 519–540. [CrossRef]
51. Zhang, J.; Li, Y.; Sun, J.; Chen, H.; Zhu, Y.; Zhao, X.; Zhang, L.C.; Wang, S.; Zhang, H.; Duan, X.; et al. Regulation of Energetic Hot Carriers on Pt/TiO₂ with Thermal Energy for Photothermal Catalysis. *Appl. Catal. B* **2022**, *309*, 121263. [CrossRef]
52. Kattel, S.; Liu, P.; Chen, J.G. Tuning Selectivity of CO₂ Hydrogenation Reactions at the Metal/Oxide Interface. *J. Am. Chem. Soc.* **2017**, *139*, 9739–9754. [CrossRef]
53. Wang, N.; Qian, W.; Chu, W.; Wei, F. Crystal-Plane Effect of Nanoscale CeO₂ on the Catalytic Performance of Ni/CeO₂ Catalysts for Methane Dry Reforming. *Catal. Sci. Technol.* **2016**, *6*, 3594–3605. [CrossRef]
54. Tavasoli, A.V.; Preston, M.; Ozin, G. Photocatalytic Dry Reforming: What Is It Good For? *Energy Environ. Sci.* **2021**, *14*, 3098–3109. [CrossRef]
55. Pan, F.; Xiang, X.; Du, Z.; Sarnello, E.; Li, T.; Li, Y. Integrating Photocatalysis and Thermocatalysis to Enable Efficient CO₂ Reforming of Methane on Pt Supported CeO₂ with Zn Doping and Atomic Layer Deposited MgO Overcoating. *Appl. Catal. B* **2020**, *260*, 118189. [CrossRef]
56. Ranjekar, A.M.; Yadav, G.D. Dry Reforming of Methane for Syngas Production: A Review and Assessment of Catalyst Development and Efficacy. *J. Indian Chem. Soc.* **2021**, *98*, 100002. [CrossRef]
57. Zhang, Z.; Zhang, Y.; Liu, L. Role and Mechanism of Calcium-Based Catalysts for Methane Dry Reforming: A Review. *Fuel* **2024**, *355*, 129329. [CrossRef]
58. Zhang, Z.Y.; Li, T.; Yao, J.L.; Xie, T.; Xiao, Q. Mechanism and Kinetic Characteristics of Photo-Thermal Dry Reforming of Methane on Pt/Mesoporous-TiO₂ Catalyst. *Mol. Catal.* **2023**, *535*, 112828. [CrossRef]
59. Xu, Z.; Park, E.D. Recent Advances in Coke Management for Dry Reforming of Methane over Ni-Based Catalysts. *Catalysts* **2024**, *14*, 176. [CrossRef]
60. Grams, J.; Ruppert, A.M. Catalyst Stability—Bottleneck of Efficient Catalytic Pyrolysis. *Catalysts* **2021**, *11*, 265. [CrossRef]
61. Study on the Critical Raw Materials for the EU 2023—Publications Office of the EU. Available online: <https://op.europa.eu/en/publication-detail/-/publication/57318397-fdd4-11ed-a05c-01aa75ed71a1/language-en> (accessed on 3 June 2024).
62. Anderson, C.G. The Production of Critical Materials as By Products. *Asp. Min. Miner. Sci.* **2018**, *2*, 532. [CrossRef]
63. García-Diéguez, M.; Pieta, I.S.; Herrera, M.C.; Larrubia, M.A.; Alemany, L.J. Improved Pt-Ni Nanocatalysts for Dry Reforming of Methane. *Appl. Catal. A Gen.* **2010**, *377*, 191–199. [CrossRef]
64. Damyanova, S.; Pawelec, B.; Arishtirova, K.; Fierro, J.L.G.; Sener, C.; Dogu, T. MCM-41 Supported PdNi Catalysts for Dry Reforming of Methane. *Appl. Catal. B* **2009**, *92*, 250–261. [CrossRef]
65. Pinheiro, A.N.; Valentini, A.; Sasaki, J.M.; Oliveira, A.C. Highly Stable Dealuminated Zeolite Support for the Production of Hydrogen by Dry Reforming of Methane. *Appl. Catal. A Gen.* **2009**, *355*, 156–168. [CrossRef]
66. Alabi, W.O. CO₂ Reforming of CH₄ on Ni-Al-Ox Catalyst Using Pure and Coal Gas Feeds: Synergetic Effect of CoO and MgO in Mitigating Carbon Deposition. *Environ. Pollut.* **2018**, *242*, 1566–1576. [CrossRef] [PubMed]
67. Grilli, M.L.; Slobozeanu, A.E.; Larosa, C.; Paneva, D.; Yakoumis, I.; Cherkezova-Zheleva, Z. Platinum Group Metals: Green Recovery from Spent Auto-Catalysts and Reuse in New Catalysts—A Review. *Crystals* **2023**, *13*, 550. [CrossRef]
68. Daily Metal Price: Cobalt Price (USD/Pound) Chart for the Last Year. Available online: <https://www.dailymetalprice.com/metalpricecharts.php?c=co&u=lb&d=240> (accessed on 7 January 2024).
69. Hu, Q.; Li, Y.; Wu, J.; Hu, Y.; Cao, H.; Yang, Y. Extraordinary Catalytic Performance of Nickel Half-Metal Clusters for Light-Driven Dry Reforming of Methane. *Adv. Energy Mater.* **2023**, *13*, 2300071. [CrossRef]
70. Banković-Ilić, I.B.; Miladinović, M.R.; Stamenković, O.S.; Veljković, V.B. Application of Nano CaO-Based Catalysts in Biodiesel Synthesis. *Renew. Sustain. Energy Rev.* **2017**, *72*, 746–760. [CrossRef]
71. Wang, L.; Pu, Z.; Shi, Y.; Wu, M.; Shi, W.; Wang, F. Photothermal Methane Dry Reforming Catalyzed by Multifunctional (Ni-Cu/CeO₂)@SiO₂ Catalyst. *ACS Sustain. Chem. Eng.* **2023**, *11*, 17384–17399. [CrossRef]
72. Wang, E.; Zhu, Z.; Li, R.; Wu, J.; Ma, K.; Zhang, J. Ni/CaO-Based Dual-Functional Materials for Calcium-Looping CO₂ Capture and Dry Reforming of Methane: Progress and Challenges. *Chem. Eng. J.* **2024**, *482*, 148476. [CrossRef]
73. Han, K.; Wang, Y.; Wang, S.; Liu, Q.; Deng, Z.; Wang, F. Narrowing Band Gap Energy of CeO₂ in (Ni/CeO₂)@SiO₂ Catalyst for Photothermal Methane Dry Reforming. *Chem. Eng. J.* **2021**, *421*, 129989. [CrossRef]
74. Yao, Y.; Li, B.; Gao, X.; Yang, Y.; Yu, J.; Lei, J.; Li, Q.; Meng, X.; Chen, L.; Xu, D. Highly Efficient Solar-Driven Dry Reforming of Methane on a Rh/LaNiO₃ Catalyst through a Light-Induced Metal-To-Metal Charge Transfer Process. *Adv. Mater.* **2023**, *35*, 2303654. [CrossRef] [PubMed]
75. Lorber, K.; Djinić, P. Accelerating Photo-Thermal CO₂ Reduction to CO, CH₄ or Methanol over Metal/Oxide Semiconductor Catalysts. *iScience* **2022**, *25*, 104107. [CrossRef]

76. Liu, H.; Li, M.; Dao, T.D.; Liu, Y.; Zhou, W.; Liu, L.; Meng, X.; Nagao, T.; Ye, J. Design of PdAu Alloy Plasmonic Nanoparticles for Improved Catalytic Performance in CO₂ Reduction with Visible Light Irradiation. *Nano Energy* **2016**, *26*, 398–404. [[CrossRef](#)]
77. Bhattar, S.; Abedin, M.A.; Kanitkar, S.; Spivey, J.J. A Review on Dry Reforming of Methane over Perovskite Derived Catalysts. *Catal. Today* **2021**, *365*, 2–23. [[CrossRef](#)]
78. Moogi, S.; Hyun Ko, C.; Hoon Rhee, G.; Jeon, B.H.; Ali Khan, M.; Park, Y.K. Influence of Catalyst Synthesis Methods on Anti-Coking Strength of Perovskites Derived Catalysts in Biogas Dry Reforming for Syngas Production. *Chem. Eng. J.* **2022**, *437*, 135348. [[CrossRef](#)]
79. Zhao, S.; Luo, Y.; Li, C.; Ren, K.; Zhu, Y.; Dou, W. High-Performance Photothermal Catalytic CO₂ Reduction to CH₄ and CO by ABO₃ (A = La, Ce; B = Ni, Co, Fe) Perovskite Nanomaterials. *Ceram. Int.* **2023**, *49*, 20907–20919. [[CrossRef](#)]
80. Costilla, I.O.; Sánchez, M.D.; Gigola, C.E. Palladium Nanoparticle's Surface Structure and Morphology Effect on the Catalytic Activity for Dry Reforming of Methane. *Appl. Catal. A Gen.* **2014**, *478*, 38–44. [[CrossRef](#)]
81. Taherian, Z.; Shahed Gharahshiran, V.; Khataee, A.; Meshkani, F.; Orooji, Y. Comparative Study of Modified Ni Catalysts over Mesoporous CaO-Al₂O₃ Support for CO₂/Methane Reforming. *Catal. Commun.* **2020**, *145*, 106100. [[CrossRef](#)]
82. Takami, D.; Ito, Y.; Kawaharasaki, S.; Yamamoto, A.; Yoshida, H. Low Temperature Dry Reforming of Methane over Plasmonic Ni Photocatalysts under Visible Light Irradiation. *Sustain. Energy Fuels* **2019**, *3*, 2968–2971. [[CrossRef](#)]
83. Fertout, R.I.; Ghelamallah, M.; Helamallah, M.; Kacimi, S.; López, P.N.; Corberán, V.C. Nickel Supported on Alkaline Earth Metal-Doped γ -Al₂O₃-La₂O₃ as Catalysts for Dry Reforming of Methane. *Russ. J. Appl. Chem.* **2020**, *93*, 289–298. [[CrossRef](#)]
84. Khan, A.A.; Tahir, M. Well-Designed 2D/2D Ti₃C₂T_{A/R} MXene Coupled g-C₃N₄ Heterojunction with in-Situ Growth of Anatase/Rutile TiO₂ Nucleates to Boost Photocatalytic Dry-Reforming of Methane (DRM) for Syngas Production under Visible Light. *Appl. Catal. B* **2021**, *285*, 119777. [[CrossRef](#)]
85. Tahir, B.; Tahir, M.; Amin, N.A.S. Photo-Induced CO₂ Reduction by CH₄/H₂O to Fuels over Cu-Modified g-C₃N₄ Nanorods under Simulated Solar Energy. *Appl. Surf. Sci.* **2017**, *419*, 875–885. [[CrossRef](#)]
86. Taherian, Z.; Gharahshiran, V.S.; Fazlikhani, F.; Yousefpour, M. Catalytic Performance of Samarium-Modified Ni Catalysts over Al₂O₃-CaO Support for Dry Reforming of Methane. *Int. J. Hydrogen Energy* **2021**, *46*, 7254–7262. [[CrossRef](#)]
87. Ranjbar, A.; Rezaei, M. Preparation of Nickel Catalysts Supported on CaO.2Al₂O₃ for Methane Reforming with Carbon Dioxide. *Int. J. Hydrogen Energy* **2012**, *37*, 6356–6362. [[CrossRef](#)]
88. Wang, C.; Sun, N.; Zhao, N.; Wei, W.; Sun, Y.; Sun, C.; Liu, H.; Snape, C.E. Coking and Deactivation of a Mesoporous Ni-CaO-ZrO₂ Catalyst in Dry Reforming of Methane: A Study under Different Feeding Compositions. *Fuel* **2015**, *143*, 527–535. [[CrossRef](#)]
89. Dama, S.; Ghodke, S.R.; Bobade, R.; Gurav, H.R.; Chilukuri, S. Active and Durable Alkaline Earth Metal Substituted Perovskite Catalysts for Dry Reforming of Methane. *Appl. Catal. B* **2018**, *224*, 146–158. [[CrossRef](#)]
90. Zhao, J.; Guo, X.; Shi, R.; Waterhouse, G.I.N.; Zhang, X.; Dai, Q.; Zhang, T. NiFe Nanoalloys Derived from Layered Double Hydroxides for Photothermal Synergistic Reforming of CH₄ with CO₂. *Adv. Funct. Mater.* **2022**, *32*, 2204056. [[CrossRef](#)]
91. Tahir, B.; Tahir, M.; Amin, N.A.S. Tailoring Performance of La-Modified TiO₂ Nanocatalyst for Continuous Photocatalytic CO₂ Reforming of CH₄ to Fuels in the Presence of H₂O. *Energy Convers. Manag.* **2018**, *159*, 284–298. [[CrossRef](#)]
92. Rao, Z.; Cao, Y.; Huang, Z.; Yin, Z.; Wan, W.; Ma, M.; Wu, Y.; Wang, J.; Yang, G.; Cui, Y.; et al. Insights into the Nonthermal Effects of Light in Dry Reforming of Methane to Enhance the H₂/CO Ratio near Unity over Ni/Ga₂O₃. *ACS Catal.* **2021**, *11*, 4730–4738. [[CrossRef](#)]
93. Boudart, M. Turnover Rates in Heterogeneous Catalysis. *Chem. Rev.* **1995**, *95*, 661–666. [[CrossRef](#)]
94. Kozuch, S.; Martin, J.M.L. "Turning over" Definitions in Catalytic Cycles. *ACS Catal.* **2012**, *2*, 2787–2794. [[CrossRef](#)]
95. Crampton, A.S.; Rötzer, M.D.; Ridge, C.J.; Yoon, B.; Schweinberger, F.F.; Landman, U.; Heiz, U. Assessing the Concept of Structure Sensitivity or Insensitivity for Sub-Nanometer Catalyst Materials. *Surf. Sci.* **2016**, *652*, 7–19. [[CrossRef](#)]
96. Vogt, C.; Kranenborg, J.; Monai, M.; Weckhuysen, B.M. Structure Sensitivity in Steam and Dry Methane Reforming over Nickel: Activity and Carbon Formation. *ACS Catal.* **2020**, *10*, 1428–1438. [[CrossRef](#)]
97. Han, J.W.; Park, J.S.; Choi, M.S.; Lee, H. Uncoupling the Size and Support Effects of Ni Catalysts for Dry Reforming of Methane. *Appl. Catal. B* **2017**, *203*, 625–632. [[CrossRef](#)]
98. Wang, Y.; Yao, L.; Wang, Y.; Wang, S.; Zhao, Q.; Mao, D.; Hu, C. Low-Temperature Catalytic CO₂ Dry Reforming of Methane on Ni-Si/ZrO₂ Catalyst. *ACS Catal.* **2018**, *8*, 6495–6506. [[CrossRef](#)]
99. Usman, M.; Wan Daud, W.M.A.; Abbas, H.F. Dry Reforming of Methane: Influence of Process Parameters—A Review. *Renew. Sustain. Energy Rev.* **2015**, *45*, 710–744. [[CrossRef](#)]
100. Yang, Y.; Chai, Z.; Qin, X.; Zhang, Z.; Muhetaer, A.; Wang, C.; Huang, H.; Yang, C.; Ma, D.; Li, Q.; et al. Light-Induced Redox Looping of a Rhodium/Cex WO₃ Photocatalyst for Highly Active and Robust Dry Reforming of Methane. *Angew. Chem. Int. Ed. Engl.* **2022**, *61*, e202200567. [[CrossRef](#)] [[PubMed](#)]
101. Yin, Q.; Shen, T.; Li, J.; Ning, C.; Xue, Y.; Chen, G.; Xu, M.; Wang, F.; Song, Y.F.; Zhao, Y.; et al. Solar-Driven Dry Reforming of Methane Using RuNi Single-Atom Alloy Catalyst Coupled with Thermal Decomposition of Carbonates. *Chem. Eng. J.* **2023**, *470*, 144416. [[CrossRef](#)]
102. Song, H.; Meng, X.; Dao, T.D.; Zhou, W.; Liu, H.; Shi, L.; Zhang, H.; Nagao, T.; Kako, T.; Ye, J. Light-Enhanced Carbon Dioxide Activation and Conversion by Effective Plasmonic Coupling Effect of Pt and Au Nanoparticles. *ACS Appl. Mater. Interfaces* **2018**, *10*, 408–416. [[CrossRef](#)] [[PubMed](#)]

103. Wu, S.; Li, Y.; Hu, Q.; Wu, J.; Zhang, Q. Photothermocatalytic Dry Reforming of Methane for Efficient CO₂ Reduction and Solar Energy Storage. *ACS Sustain. Chem. Eng.* **2021**, *9*, 11635–11651. [[CrossRef](#)]
104. Zhang, Z.-Y.; Zhang, T.; Liang, W.P.; Bai, P.W.; Zheng, H.Y.; Lei, Y.; Hu, Z.; Xie, T. Promoted Solar-Driven Dry Reforming of Methane with Pt/Mesoporous-TiO₂ Photo-Thermal Synergistic Catalyst: Performance and Mechanism Study. *Energy Convers. Manag.* **2022**, *258*, 115496. [[CrossRef](#)]
105. Zhang, Z.-Y.; Zhang, T.; Wang, R.-K.; Yu, B.; Tang, Z.-Y.; Zheng, H.-Y.; He, D.; Xie, T.; Hu, Z. Photo-Enhanced Dry Reforming of Methane over Pt-Au/P25 Composite Catalyst by Coupling Plasmonic Effect. *J. Catal.* **2022**, *413*, 829–842. [[CrossRef](#)]
106. Zhang, J.; Wang, L.; Zhao, X.; Shi, L.; Chen, H.; Zhang, S.; Zhang, P.; Wang, S.; Zhang, L.; Wang, Y.; et al. The Nature of Active Sites for Plasmon-Mediated Photothermal Catalysis and Heat-Coupled Photocatalysis in Dry Reforming of Methane. *Energy Environ. Mater.* **2023**, *6*, e12416. [[CrossRef](#)]
107. Zhao, Y.X.; Yang, B.; Li, H.F.; Zhang, Y.; Yang, Y.; Liu, Q.Y.; Xu, H.G.; Zheng, W.J.; He, S.G. Photoassisted Selective Steam and Dry Reforming of Methane to Syngas Catalyzed by Rhodium–Vanadium Bimetallic Oxide Cluster Anions at Room Temperature. *Angew. Chem. Int. Ed.* **2020**, *59*, 21216–21223. [[CrossRef](#)] [[PubMed](#)]

Disclaimer/Publisher’s Note: The statements, opinions and data contained in all publications are solely those of the individual author(s) and contributor(s) and not of MDPI and/or the editor(s). MDPI and/or the editor(s) disclaim responsibility for any injury to people or property resulting from any ideas, methods, instructions or products referred to in the content.